A Unified Framework for Characterization of Mode and Spike Routes to Rotating Stall

by

Marcos A. Logrono

B.S., University of Puerto Rico - Mayagüez, (Highest Honors), 2021

Submitted to the Department of Aeronautics and Astronautics
in partial fulfillment of the requirements for the degree of

MASTER OF SCIENCE IN AERONAUTICS AND ASTRONAUTICS

at the

MASSACHUSETTS INSTITUTE OF TECHNOLOGY

February 2024

Authored by:	Marcos A. Logrono Department of Aeronautics and Astronautics January 12, 2024
Certified by:	Edward M. Greitzer H. N. Slater Professor of Aeronautics and Astronautics, Thesis Supervisor
Certified by:	Zoltán S. Spakovszky T. Wilson Professor of Aeronautics and Astronautics, Thesis Supervisor
Accepted by:	Jonathan P. How R. C. Maclaurin Professor of Aeronautics and Astronautics Chair, Graduate Program Committee

A Unified Framework for Characterization of Mode and Spike Routes to Rotating Stall

by

Marcos A. Logrono

Submitted to the Department of Aeronautics and Astronautics
on January 12, 2024 in partial fulfillment of the requirements for the degree of

MASTER OF SCIENCE IN AERONAUTICS AND ASTRONAUTICS

ABSTRACT

In this thesis, we characterize modal and spike-type rotating stall inception for an isolated rotor using a low order, non-linear actuator disk model. The actuator disk representation is capable of capturing stall inception behavior given an axisymmetric total-to-static pressure rise characteristic. A parametric study of the effect of the derivative of the total-to-static pressure rise with respect to flow coefficient has been carried out to (i) define the links between the computed behavior of circumferentially propagating flow disturbances and those of established linearized analyses and (ii) describe both modes and spikes as different regimes of the same dynamical framework.

The results of the parametric study show three distinct regimes for the non-dimensional compressor characteristics examined. For total-to-static pressure rise characteristic slopes below 0.2, exponentially growing sinusoidal disturbances lead to the onset of rotating stall with growth time scales on the order of ten rotor revolutions. This behavior is characteristic of what is known as modal inception, or *modes*. For pressure rise slopes above 0.4, disturbances with no sinusoidal structures and with magnitudes of order of the mean axial flow were observed before the onset of rotating stall. The growth time scales of these disturbances were on the order of a rotor revolution. This behavior is characteristic of *spikes*. For pressure rise slopes between 0.2 and 0.4, both behaviors were observed. These results suggest a continuous transition between modal and spike inception, contrary to the description as two distinct phenomena.

Thesis supervisor: Edward M. Greitzer
Title: H. N. Slater Professor of Aeronautics and Astronautics

Thesis supervisor: Zoltán S. Spakovszky
Title: T. Wilson Professor of Aeronautics and Astronautics

Acknowledgments

The completion of this work wouldn't have been possible without the support of many. First, I would like to thank my research advisors, Professor Greitzer and Professor Spakovszky, whose expertise, knowledge, and guidance were vital for this research. I am deeply grateful for their support, and from them I take important lessons that will help me on my upcoming PhD work.

I would also like to mention Professor Graham Pullan and Dr. Sam Grimshaw from the Whittle Laboratory. The documentations provided by Graham on how to run and use TBLOCK greatly helped during the first few months of my research. Also, our virtual group meetings between MIT Gas Turbine Lab and Whittle Lab provided for many insightful and engaging discussions.

To my research collaborators, Maranda Cherry, Dr. Abhishek Mishra, and Dr. Marshall Galbraith, you all worked on this project at different points during my time at GTL, and I am very grateful for the support you all provided. I also want to acknowledge the amazing students, faculty, and staff at GTL that made me feel welcome from the moment I stepped in at MIT. Whether it was going for the occasional lunch break or at the weekly social hours, I enjoyed spending time and getting to meet you all.

To my friends from Puerto Rico, to the community we have built in Boston that became like my second family, to my best friend Gustavo who has been there since the beginning of my academic journey, and to my partner Linda, thank you for your love and support throughout the writing of this thesis.

To my family, Miguel, Camile, Mikey, and my dear mother Dayanara - *los amo, esto se lo dedico a ustedes.*

Contents

List of Figures

Chapter 1

Introduction

The flow in an axial compressor at design conditions is nominally steady and axisymmetric. When the flow is reduced from the design point, however, the axisymmetric flow can become unstable, leading to large amplitude transient motions of two different kinds, one known as surge, the other as rotating stall [1]. Surge is characterized by variations in overall system mass flow. In fully developed rotating stall, the mass flow is constant in time, and there are regions of reduced flow that propagate around the annulus in the direction of blade rotation, with speeds typically between 20 and 50 percent of rotor speed.

The present work focuses on descriptions of the *inception of rotating stall*. This inception occurs when there are conditions that create a break in the symmetry of the flow, with growth of circumferentially non-uniform velocity and pressure perturbations. The stall inception regime is thus the growth of small-amplitude perturbations that lead to large amplitude, fully developed rotating stall.

Two distinct routes to rotating stall have been discussed in the literature [1]. The first is the growth of small amplitude perturbations with length scale comparable to the compressor circumference. The term "modes" or "modal oscillations" have been used to describe these motions, which appear as exponentially growing sinusoidal waves with growth time scales on the order of tens of rotor revolutions. Modes have been described by linearized two-

dimensional analyses, for example for an isolated rotor, by Stenning [2] and Spakovszky [3] using two-dimensional actuator disk approximations. The analyses yield the eigenvalues of the dynamical system, giving the growth and propagation rates of the individual harmonics. Discussion of rotating stall models will be presented in Chapter 2.

A second route to stall inception, observed in experiments and CFD calculations [4][5][6], is through the appearance of a small length scale disturbance, on the order of one or several blade pitches, that propagates and leads to fully developed rotating stall in a time scale of order of one rotor revolution. This route is known as *spike* inception, because of the spike-like wave form seen in velocity or pressure traces. The initial propagation rate of spike-type disturbances is typically 60 to 80 percent of rotor frequency, slowing to 20 to 50 percent when the rotating stall is fully developed.

1.1 Thesis Scope

In this thesis we focus on stall inception behavior which suggests that both modes and spikes can be brought together under one overarching description. Based on previous actuator disk studies of rotating stall inception [7], the hypothesis is that modes and spikes are different regimes of rotating stall inception that we can describe with the same low-order dynamical framework. We assess the effect of the derivative of the axisymmetric total-to-static pressure rise, with respect to flow coefficient, on the rotating stall inception behavior and develop the conditions associated with modes and with spikes.

1.2 Contributions

The main contributions of this thesis are:

- The occurrence of modal and of spike inception of rotating stall is shown to be determined by the slope of the non-dimensional inlet total to exit static pressure rise

characteristic ($\frac{\partial \psi_{TS}}{\partial \phi}$), in agreement with results obtained by Pullan [8]. For the parameters examined, modal inception is observed for axisymmetric pressure rise slopes less than 0.2 ($\frac{\partial \psi_{TS}}{\partial \phi} < 0.2$), whereas spike disturbances are found for slopes $\frac{\partial \psi_{TS}}{\partial \phi} > 0.4$. These results imply the existence of a continuous transition between modes and spikes.

- For spike inception, increasing the slope of the pressure rise characteristic increases the differences between the growth rates from the linear models [2][3] and those from actuator disk calculations. This suggests that linear models are insufficient for describing the higher slope cases, where spike inception was observed for the actuator disk calculations.

Chapter 2

Background

In this chapter we present existing information about modes and spikes with the aim of establishing a connection between these two phenomena. An overview of the characteristics and behaviors of these two stall inception routes is presented, including examples of the circumferential structures of the axial velocity or pressure disturbances associated with modes and spikes. We also review the linearized approaches for analyzing the perturbations to show how the solutions connect to mean flow variables and to serve as a basis to categorize whether modes or spikes are observed, based on the results described in Chapter 4.

2.1 Literature review

Stall inception was first described by Emmons et al. [9] using a linearized analysis of two-dimensional, small amplitude perturbations to a cascade with uniform background flow. Emmon's analysis connected the growth of a rotating disturbance relative to a stationary probe with the behavior of boundary layer parameters (blockage). Stenning [2] expanded on this linear analysis by linking the propagation speed to the mean flow pressure rise coefficient. Stenning also showed that the instability point occurs at the peak of the total-to-static pressure rise characteristic (as first obtained by Dunham [10]).

Experimental work in the 1990's by Day [4] presented evidence for the existence of the

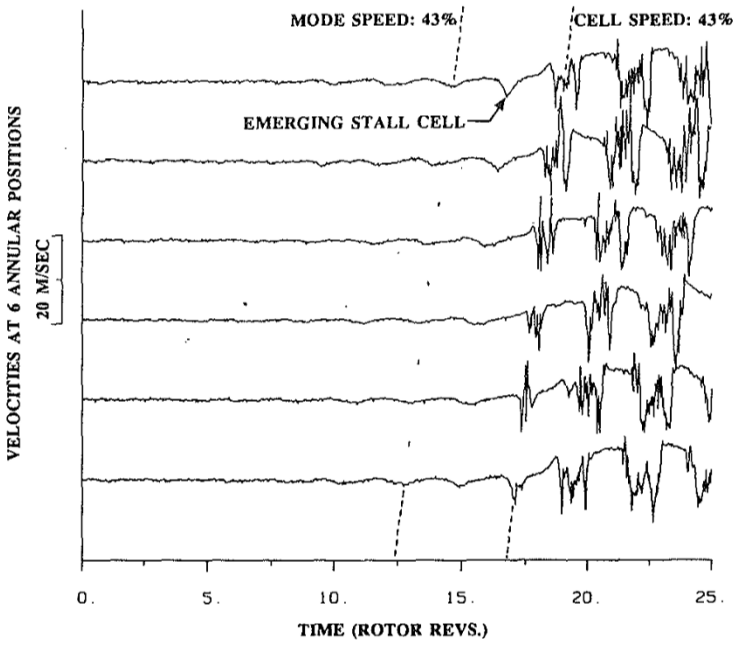

Figure 2.1: Axial velocity perturbation traces from a single stage compressor showing modal oscillations leading to stall cell formation [4].

two stall inception routes we now call modes and spikes. Measurements of upstream axial velocity for a single and four stage compressor rig from that study are shown in this section to highlight the features of modes and spikes.

2.1.1 Modal Inception

The propagating disturbances known as modes are characterized by sinusoidal circumferential non-uniformities with length scales that can be up to the compressor circumference. Initially, the amplitude of the modal oscillations is several percent of the mean flow velocity or less [5] and exhibits exponential growth.

Modal oscillations are typically present tens of rotor revolutions before the rotating stall is fully developed. Additionally, the modal disturbance phase velocity (or rotation rate) is close to the speed of the fully developed stall cell [4][5]. Figure 2.1 shows an example of modal inception, in which upstream hot-wire measurements indicate a growing modal oscillation travelling at 43% rotor speed, leading to the formation of a stall cell at the same speed [4].

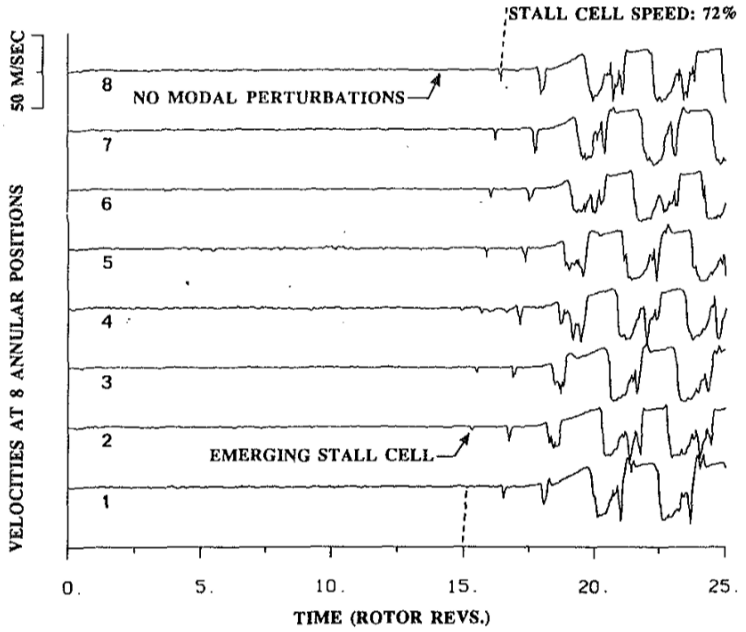

Figure 2.2: Axial velocity perturbation traces from a four stage compressor showing a spike that leads to rotating stall with no observed previous oscillations [4].

2.1.2 Spike Inception

Spike-type stall inception was first reported by Day [4]. The length scale of spike disturbances was one to several blade pitches, with initial rotation rates around 70% of the rotor speed evolving into fully developed stall cells rotating at 20 to 50% of the rotor speed. The amplitude of the spike disturbance when first detected was substantially larger than that of a mode [6] (see Figure 2.1). For spikes, the time scale from initial growth to stall cell formation was found to be one to several revolutions, as in Figure 2.2, where the spike initially propagates at 72% rotor speed and evolves into a rotating stall cell, at 38% rotor speed, within two revolutions [4].

Spikes have also been observed to occur simultaneously with modes, as in Figure 2.3 [5]. In the situation shown, modal waves caused flow separation at the tip region of the first rotor blade of a four stage compressor, and the transition to rotating stall then occurred via the spike disturbance. Spikes thus appeared to be localized phenomena that emerged over an individual blade [1].

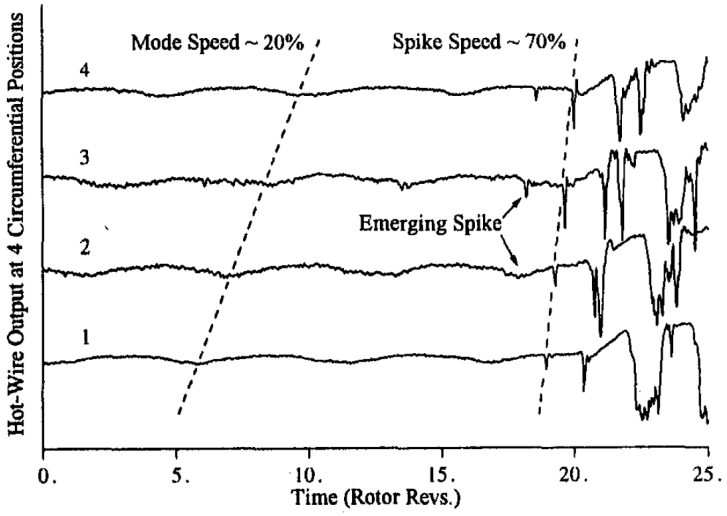

Figure 2.3: Spike disturbance developing after the appearance of axial velocity modal perturbations for a four stage compressor [5].

2.1.3 Criteria for Modes and Spikes

Camp and Day [5] proposed an explanation for why some compressors experience modal inception and others develop spikes. Their idea was based on observations that modal oscillations develop when the slope of the overall total-to-static pressure rise characteristic at the stall point is zero or slightly positive, whereas spikes originated at a negative pressure rise slope, when a critical value of rotor incidence angle was reached. Camp and Day proposed that if the peak of the total-to-static pressure rise characteristic was reached before the critical rotor incidence angle for a given compressor, modes will develop. If the critical rotor incidence angle was reached to the right of the peak ($\frac{\partial \psi_{TS}}{\partial \phi} < 0$), however, spikes will appear.

The two situations are shown in Figure 2.4. This idea was the first statement that gave insight into the relationship between the different stall inception routes and was followed by Pullan et. al who focused on describing the physical mechanisms behind the formation of spikes through a computational model of a compressor rotor blade row [6].

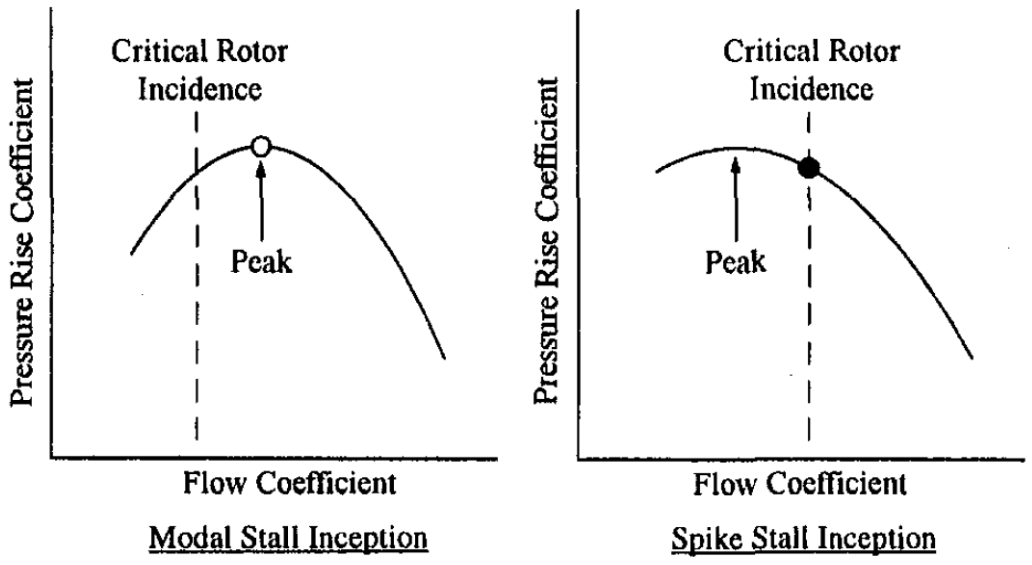

Figure 2.4: Criteria for modes and spikes based on critical rotor incidence and pressure rise characteristic slope [5].

2.2 Linearized Approach to Stall Inception

An useful introduction to approaches to stall inception modeling is the linear analysis of Stenning [2], which presents criteria for compressor instability and propagation speed. In the original reference, downstream pressure perturbations are neglected, and only conditions at the neutral stability point are considered. In Appendix A Stenning's model is extended to include these two effects.

Spakovszky presents a modular approach for compressor instabilities [3], with blade rows and other compressor components modeled through "transmission matrices" containing linearized descriptions of their behaviors. Spakovszky's analysis assumes an ideal pressure rise characteristic with loss coefficient curves to provide the actual compressor pressure rise. It also includes unsteady blade passage effects, which is useful because these are in the computational framework to be described in Chapter 3.

Spakovszky gives a closed form solution for the eigenvalues for an isolated rotor in terms of the derivative of the loss coefficient curve with respect to upstream flow angle. In this

section, the analysis is presented in terms of the slope of the total-to-static pressure rise characteristic.

2.2.1 Spakovszky's Isolated Rotor Model

Spakovszky's analysis is carried out in the absolute frame, as in Figure 2.5.

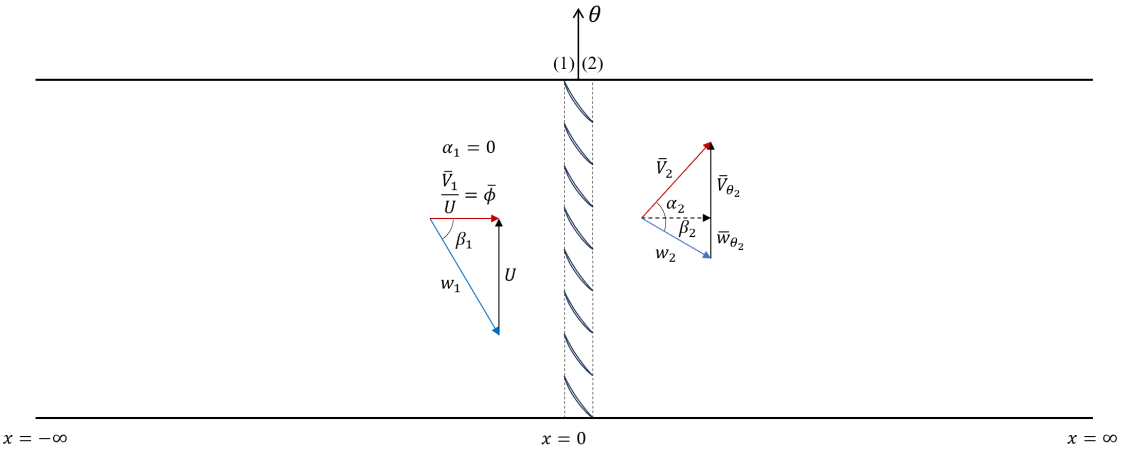

Figure 2.5: Isolated rotor geometry to Spakovszky's analysis [3].

Incompressible and inviscid flow is assumed, with the upstream flow irrotational. Stations 1 and 2 correspond to the upstream and downstream edges of the blade row. The rotor speed $U = \Omega R$ is in the direction of the circumferential coordinate θ. The mean flow approaches the rotor with zero inlet swirl and leaves the blade row at a specified relative exit flow angle β_2, which is constant. Spakovszky considers angles in the direction of rotation as positive, so relative flow angles (β) are negative. The effects of acceleration of the flow within the blade passage on the blade row pressure rise are included using a rotor fluid inertia parameter

$$\lambda = \frac{c_x}{R\cos^2\gamma}. \tag{2.1}$$

In Equation (2.1) c_x is the axial chord, and γ the blade stagger angle. The local, instanta-

neous blade row total to static pressure rise condition is given as [11]

$$\frac{p_2 - p_{t1}}{\rho U^2} = \psi_{TS}(\phi) - \lambda \left(\frac{\partial \phi}{\partial \theta} - \frac{\partial \phi}{\partial \tau} \right), \tag{2.2}$$

where $\phi = \frac{v_x}{U}$ is the flow coefficient, $\tau = \frac{tU}{R}$ the non-dimensional time, and ψ_{TS} the quasi-steady total-to-static pressure rise characteristic. Spakovszky also defines a blade row pressure loss L_R

$$L_R(\phi) = \psi^I_{TS}(\phi) - \psi_{TS}(\phi), \tag{2.3}$$

where ψ^I_{TS} is the ideal total-to-static pressure rise characteristic. From the Euler equation, the ideal total-to-total pressure rise is

$$\psi^I_{TT} = 1 + \phi \left(\tan \beta_2 - \tan \alpha_1 \right). \tag{2.4}$$

Converting Equation (2.2) into total-to-total form and using Equation (2.4) for the ideal pressure rise yields a pressure matching condition

$$P_{t2} - P_{t1} = 1 + \phi \left(\tan \beta_2 - \tan \alpha_1 \right) - L_R - \lambda \left(\frac{\partial \phi}{\partial \theta} - \frac{\partial \phi}{\partial \tau} \right), \tag{2.5}$$

where $P_{t2} - P_{t1}$ is the stagnation pressure rise for the blade row non-dimensionalized by ρU^2. The pressure loss L_R is the same in total-to-total and total-to-static terms.

In addition to Equation (2.5), two other matching conditions are needed, for the isolated rotor, to express mass conservation and constant exit flow angle:

$$\phi_1 = \phi_2, \tag{2.6}$$

$$V_{\theta 2} = 1 + \phi_2 \tan \beta_2. \tag{2.7}$$

In Equation (2.7), $V_{\theta 2}$ is the exit circumferential velocity. Linearizing Equations (2.5) to (2.7), applying the Laplace transform, and solving for s yields the eigenvalues of the isolated

rotor system as

$$\sigma_n = \frac{\tan\beta_2 + \frac{\partial L_R}{\partial \tan\beta_1}\frac{\tan\beta_1}{\phi} - \phi\left(1+\tan^2\alpha_2\right) + \tan\alpha_2}{\lambda + \frac{2}{n}}, \tag{2.8}$$

$$\omega_n = \frac{\frac{\partial L_R}{\partial \tan\beta_1}\frac{1}{\phi} + n\lambda + 1}{\lambda + \frac{2}{n}}. \tag{2.9}$$

Equations (2.8) and (2.9) are obtained assuming the mean flow inlet swirl is zero. To express these solutions in terms of ψ_{TS}, the gradient term can be expressed using the derivative of the loss with respect to the flow coefficient as

$$\frac{\partial L_R}{\partial \tan\beta_1} = \frac{1}{\tan^2\beta_1}\frac{\partial L_R}{\partial \phi}. \tag{2.10}$$

The mean ideal total-to-total pressure rise can be converted to a total-to-static coefficient by subtracting the mean exit dynamic head:

$$\psi_{TS}^I = \psi_{TT}^1 - \frac{1}{2}\left(\frac{V_2}{U}\right)^2. \tag{2.11}$$

Because $\tan\alpha_1 = 0$ for the mean flow, the expression for the ideal total-to-static pressure rise in terms of ϕ is

$$\psi_{TS}^I = \frac{1}{2}\left(1 - \phi^2\left(1+\tan^2\beta_2\right)\right). \tag{2.12}$$

Plugging Equation (2.12) into Equation (2.3) and taking the derivative with respect to flow coefficient gives

$$\frac{\partial L_R}{\partial \phi} = -\left(\phi\left(1+\tan^2\beta_2\right) + \frac{\partial \psi_{TS}}{\partial \phi}\right). \tag{2.13}$$

Thus, the loss gradient term becomes

$$\frac{\partial L_R}{\partial \tan\beta_1} = -\frac{1}{\tan^2\beta_1}\left(\phi\left(1+\tan^2\beta_2\right) + \frac{\partial \psi_{TS}}{\partial \phi}\right). \tag{2.14}$$

By considering that for the mean flow $\phi = -\frac{1}{\tan\beta_1}$, Equation (2.14) can be used to express

Spakovszky's eigenvalue solutions for an isolated rotor system in terms of ϕ, $\tan\beta_2$, and the derivative of ψ_{TS} with respect to flow coefficient. After some re-arrangements, the growth and rotation rates for the isolated rotor are expressed as

$$\sigma_n = \frac{\frac{\partial \psi_{TS}}{\partial \phi}}{\lambda + \frac{2}{n}}, \tag{2.15}$$

$$\omega_n = \frac{2\psi_{TS}^I - \frac{\partial \psi_{TS}}{\partial \phi}\phi + n\lambda}{\lambda + \frac{2}{n}}. \tag{2.16}$$

The inclusion of unsteady blade passage effects reduces the growth rates of the pre-stall harmonics but does not affect the instability point, which occurs at $\frac{\partial \psi_{TS}}{\partial \phi} = 0$. The pre-stall waves travel in the direction of the isolated rotor rotation. In Appendix A, Equations (2.15) and (2.16) are compared with the solutions from Stenning's analysis.

2.2.2 Moore-Greitzer Axisymmetric Pressure Rise Curve

To plot an example for Equations (2.15) and (2.16), we can use the Moore-Greitzer cubic axisymmetric curve [12] for the total-to-static pressure rise characteristic:

$$\psi_{TS}(\phi) = \psi_0 + H\left(1 + \frac{3}{2}\left(\frac{\phi}{W} - 1\right) - \frac{1}{2}\left(\frac{\phi}{W} - 1\right)^3\right), \tag{2.17}$$

where ψ_0 is the axisymmetric shut-off value and H and W are parameters corresponding to ψ and ϕ values for the peak pressure rise ($\frac{\partial \psi_{TS}}{\partial \phi} = 0$). The ψ and ϕ values at the peak of the cubic characteristic are related to H and W as

$$\psi_{peak} = 2H + \psi_0, \tag{2.18}$$

$$\phi_{peak} = 2W. \tag{2.19}$$

We choose $\psi_0 = 0$, $H = 0.1025$, and $W = 0.185$ to describe our cubic characteristic and let the exit flow angle be $\beta_2 = 51.45$ degrees[1]. The ideal total-to-total pressure rise ψ_{TT}^I, ideal total-to-static pressure rise ψ_{TS}^I, and steady state axisymmetric cubic characteristic ψ_{TS} using the above parameters are plotted in Figure 2.6, as is the loss coefficient as a function of ϕ. Growth and rotation rates for this axisymmetric pressure rise characteristic are given in Appendix C.

[1]Mean values for cubic pressure rise taken from Prof. Pullan test cases in [7]

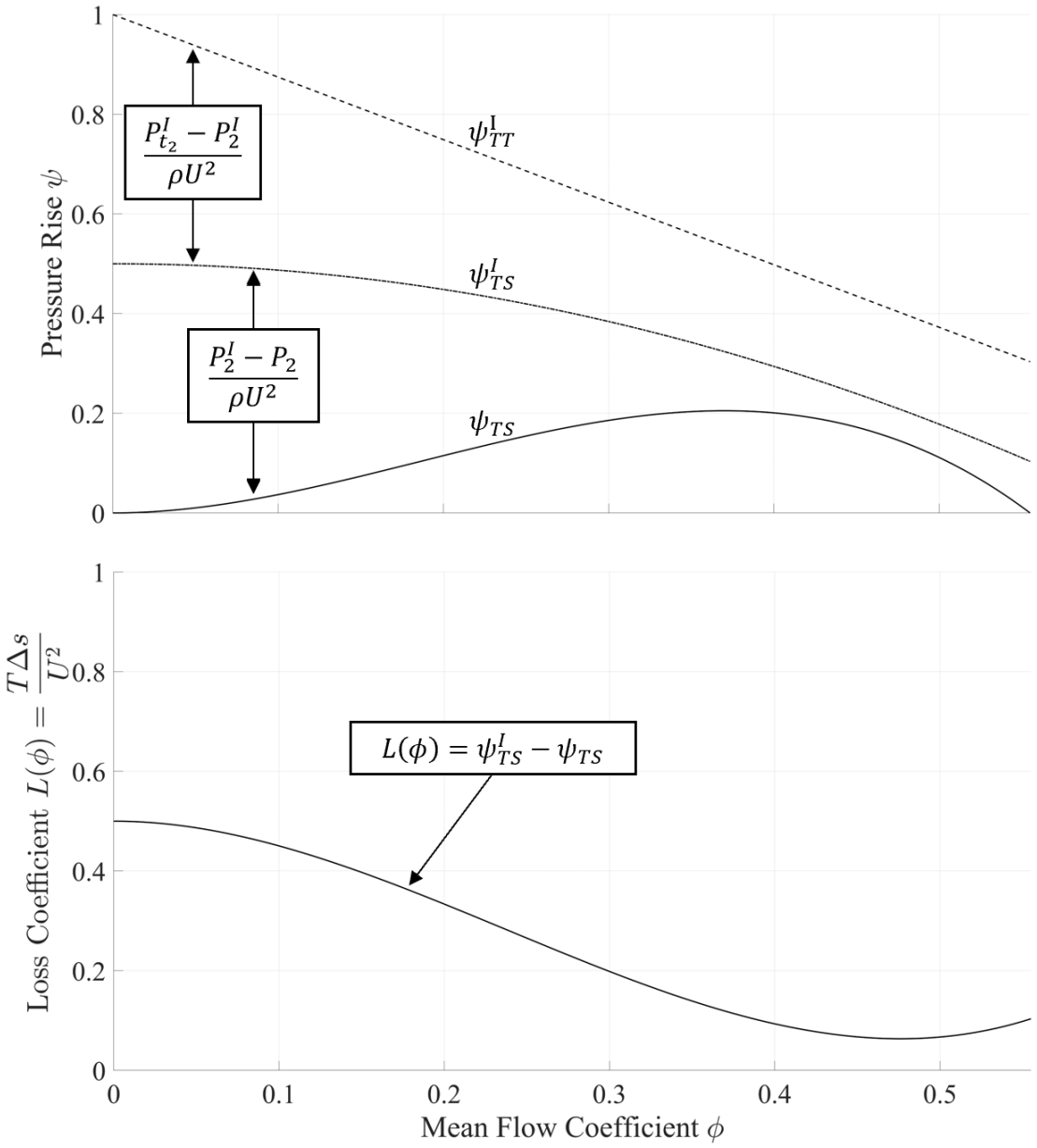

Figure 2.6: Axisymmetric pressure rise and loss curves for Moore-Greitzer characteristic defined in Section 2.2.2.

Chapter 3

Computational Framework

Chapter 2 described a two-dimensional linear analysis of sinusoidal unsteady perturbations in an incompressible flow. The growth and rotation rates of these perturbations are a function of the mean flow quantities. In particular, the growth rate of the n-th harmonic is equal to the product of the slope of the mean total-to-static pressure rise and the harmonic number. We will assess the utility of this relation compared to a computational non-linear actuator disk model [7]. We also attempt to draw connections between the total-to-static pressure rise slope and the emergence of modal or spike stall inception using a series of simulations. In this chapter we describe the computational framework used for these transient simulations and the signal processing to visualize the pre-stall harmonics. The computational procedure is for compressible flow but, because of the low mach numbers considered here ($M_{Tip} \approx 0.2$), the density increase is negligible during stall inception, and incompressible analyses are appropriate for comparison.

3.1 Actuator Disk Flow Model

A schematic of the computational domain used is presented in Figure 3.1. As in the linear analysis described previously in Chapter 2, the blade row is replaced by an actuator disk. The duct downstream of the disk has a constant area nozzle at the outlet as in Figure 3.1.

The length of each duct is twice the circumference of the disk, so that asymmetric pressure influences from the outlet boundary conditions are negligible. The domain has a hub-to-tip radius ratio of 0.9999 to give a geometry that is quasi-two dimensional. The operating points of the actuator disk are set by changing the nozzle exit static pressure.

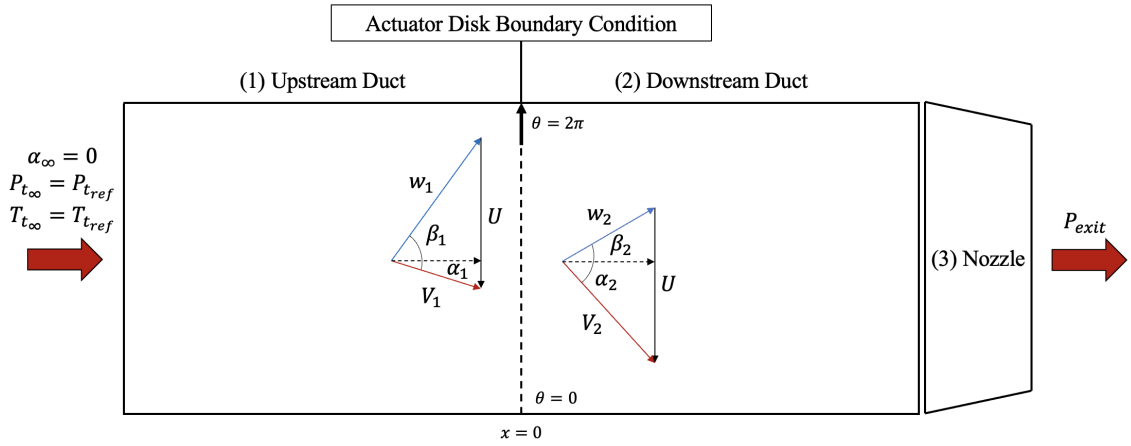

Figure 3.1: TBLOCK actuator disk model schematic (not to scale).

The solver algorithm for this model, referred to as TBLOCK [7], is based on the procedures presented in Joo and Hynes [13] in which the unsteady Euler equations are solved. For the compressible analysis, there are five matching conditions required across the actuator disk, applied at each radial and circumferential node:

1. Conservation of Mass

$$(\rho V_x)_1 = (\rho V_x)_2 \tag{3.1}$$

2. Conservation of Radial Momentum

$$V_{r_1} = V_{r_2} \tag{3.2}$$

3. Conservation of Rothalpy

$$\left(h_{t_{rel}} - \frac{U^2}{2}\right)_1 = \left(h_{t_{rel}} - \frac{U^2}{2}\right)_2 \tag{3.3}$$

4. Specification of Relative Exit Flow Angle

$$\beta_2 = f(r) \tag{3.4}$$

5. Loss Coefficient

$$\zeta = f(\beta_1) = \frac{T\Delta s}{\frac{1}{2}w_1^2} \tag{3.5}$$

Conditions 1 to 3 correspond to the equations of motion, condition 4 sets a constant exit flow angle at each radial node, and the 5-th condition is the input axisymmetric loss coefficient, entropy rise non-dimensionalized by upstream dynamic pressure as a function of inlet relative flow angle, β_1.

The TBLOCK[1] actuator disk model contains a compressible flow solver routine for unsteady flow field computations. This routine, along with the mesh geometry used in this thesis, is given in Appendix B.

3.1.1 Estimation of Axisymmetric Loss Coefficient

Assuming zero inlet swirl α_1, the axisymmetric loss coefficient curves have been derived from the total-to-static pressure rise characteristics. The non-dimensional loss is

$$\frac{T\Delta s}{U^2} = \frac{\Delta h_t}{U^2} - \frac{\Delta p_t}{\rho U^2}. \tag{3.6}$$

The ideal work coefficient, $\frac{\Delta h_t}{U^2}$, is the isentropic total-to-total pressure rise in Equation (2.4). Writing the total pressure rise and work done in terms of total-to-static pressure and rearranging, the loss coefficient in Equation (3.5) can be written as a function of the pressure rise characteristic:

$$\frac{T\Delta s}{\frac{1}{2}w_1^2} = \frac{T\Delta s}{\frac{1}{2}\bar{w}_x^2 + \frac{1}{2}U^2} = \frac{2}{1+\phi^2}\left(\psi_{TS}^I - \psi_{TS}\right) \tag{3.7}$$

[1]TBLOCK source codes provided by Prof. Pullan from the Whittle Lab at Cambridge University.

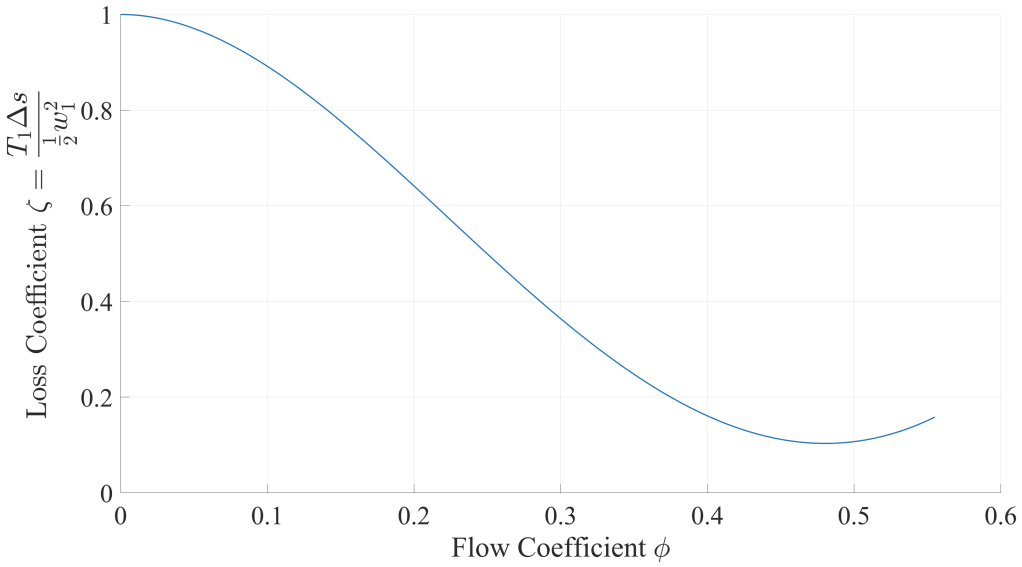

Figure 3.2: Loss coefficient for Moore-Greitzer example characteristic.

Using the ideal total-to-static pressure rise from Equation (2.11), we obtain the axisymmetric loss coefficient curve used for the TBLOCK calculations, in Figure 3.2, corresponding to the Moore-Greitzer [12] cubic axisymmetric curve from Section 2.2.2.

3.2 Spatial Fourier Analysis for Traveling Waves

The TBLOCK calculations yield circumferentially travelling disturbances and we have carved out a spatial Fourier analysis to capture the structure of the pressure and velocity perturbations through time. The actuator disk domain contains 101 evenly spaced points, with the first and last connected through periodic boundary conditions. If N is the number of circumferential points, N must meet the Nyquist criterion such that $N \geq 2n$, where n is the number of harmonics to be captured. Thus, for $N = 100$, we can capture up to the 50-th harmonic of the pressure or velocity disturbance. Following the framework of Garnier [14][15], the spatial Fourier coefficient of the $n - th$ harmonic is given by

$$\widetilde{\phi}(n, \tau) = \frac{1}{N} \sum_{k=1}^{N} \phi_k(\tau) \exp\left[-\frac{2\pi i n k}{N}\right], \tag{3.8}$$

where ϕ_k is the non-dimensional axial velocity at probe number k, and non-dimensional time τ. The spatial Fourier coefficients (SFC) contain the information on the harmonic wave amplitude and position, and we can find the growth and rotation rates for each harmonic assuming the Fourier coefficients are of the form

$$\widetilde{\phi}(n,\tau) = A_n e^{s_n \tau} \tag{3.9}$$

where $s_n = \sigma_n - i\omega_n$.

In Chapter 4 we will investigate the behavior of the spatial Fourier coefficients for different axisymmetric pressure rise characteristics.

Chapter 4

Effect of Compressor Pressure Rise Slope on Rotating Stall Inception

In this chapter we describe the relationship between the slope of the mean total-to-static pressure rise and the stall inception process. Previous calculations have shown that throttling the actuator disk to different points past the neutral point ($\frac{\partial \psi_{TS}}{\partial \phi} = 0$) yields different stall inception behaviors [8]. For example, a second harmonic disturbance was shown to dominate the inception of rotating stall for larger throttle steps since, for a cubic pressure rise, increasing the throttle step pushes the operating point towards a steeper positive slope, in agreement with the linear analysis of Chapter 2.

A series of TBLOCK calculations were thus done using total-to-static pressure rise characteristics with constant slope for the positive flow coefficient range, to eliminate the variation of the pressure rise slope with operating point and allow us to isolate the effects of slope on stall inception. The results of these calculations are compared with the linear analysis to categorize whether modes or spikes are observed for a given slope.

4.1 TBLOCK Calculation Setup

4.1.1 Input Parameters

For consistency, the following parameters were used for all the cases considered in this chapter:

- Rotor fluid inertia parameter (see Equation (2.1)): $\lambda = 0.2$
- Constant exit flow angle: $\beta_2 = 51.45°$
- Circumferential inlet flow variation ($\Delta\beta_1$): Root-mean-square = 0.01

The exit flow angle corresponds to the example in Chapter 2. A circumferentially varying inlet flow angle disturbance $\Delta\beta_1$ rotating at blade speed U was applied for the transient calculations to provide small initial rotating disturbances from which the different harmonics grow. A random distribution of inlet flow angle variation with a root-mean-square (RMS) of 0.01 degrees was applied at the mesh nodes (see Section B.1 of Appendix B). The distribution is shown in Figure 4.1.

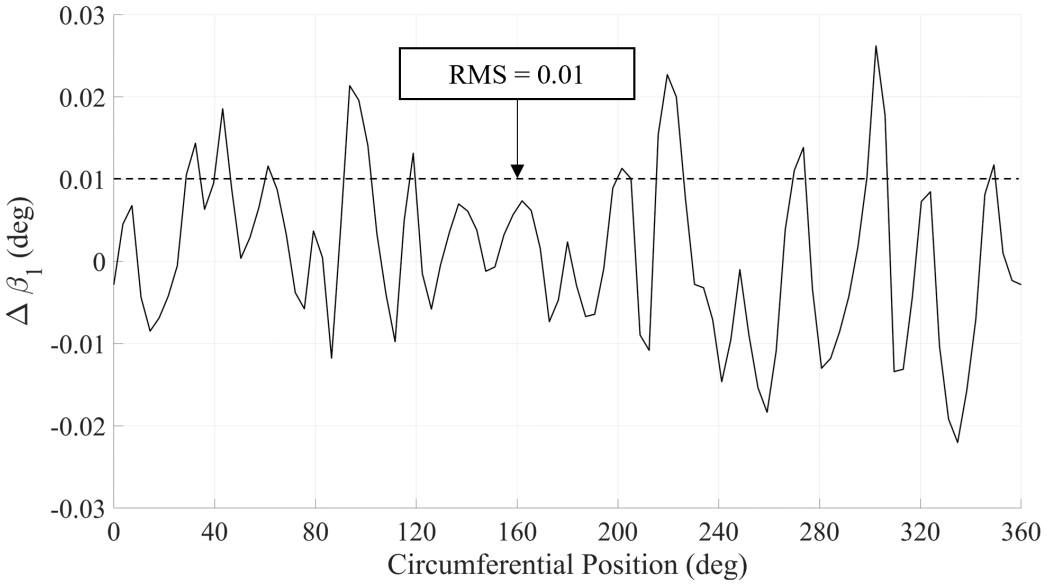

Figure 4.1: Inlet flow angle variation for TBLOCK calculations

4.1.2 Simulation Procedure

The procedure depicted in Figure 4.2 was followed for all the TBLOCK simulations described in this chapter.

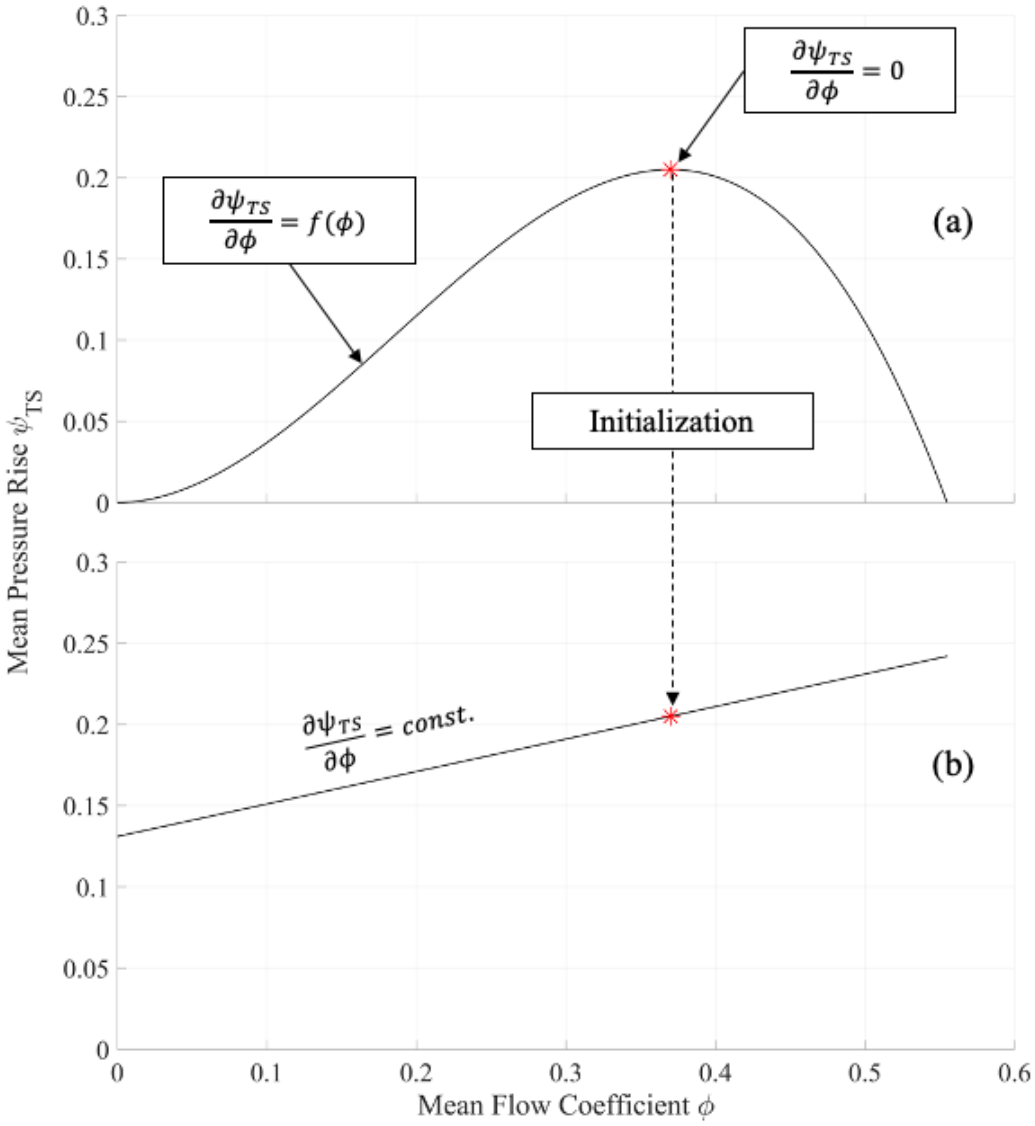

Figure 4.2: TBLOCK calculation setup showing: (a) Steady solution at the peak of the cubic pressure rise used for the computation's initialization; (b) Point of initialization for constant slope pressure rise cases.

For all cases, the mean pressure rise characteristic was constant along the radial direction. A stable solution at the peak of the cubic pressure rise was first found, as in Figure 2.6 which

shows non-dimensional pressure rise, ψ_{TS}, versus flow coefficient, ϕ. This stable solution is then used to initialize the unsteady calculations using the constant slope characteristics that cross the peak of the cubic curve as in Figure 4.2. The flow is unstable on this straight-line characteristic because $\frac{\partial \psi_{TS}}{\partial \phi} > 0$, and we can capture the stall inception transient for different mean pressure rise slopes. This procedure is based on ideas presented by Prof. Pullan [7][8].

4.2 Mean Pressure Rise Case Matrix

Figure 4.3 shows the constant slope characteristics that are included in this study. Spikes have been observed for a pressure rise slope of 0.4[7][8], and a range of slopes from 0.04 to 0.6 were thus considered. The linearized two-dimensional analysis states that the growth rate of a given harmonic is equal to the product of the slope of the mean total-to-static pressure rise characteristic and the harmonic number n. All the characteristics considered have a constant slope as a function of ϕ, so the growth of each harmonic is expected to be constant with flow coefficient, at least in the linear regime.

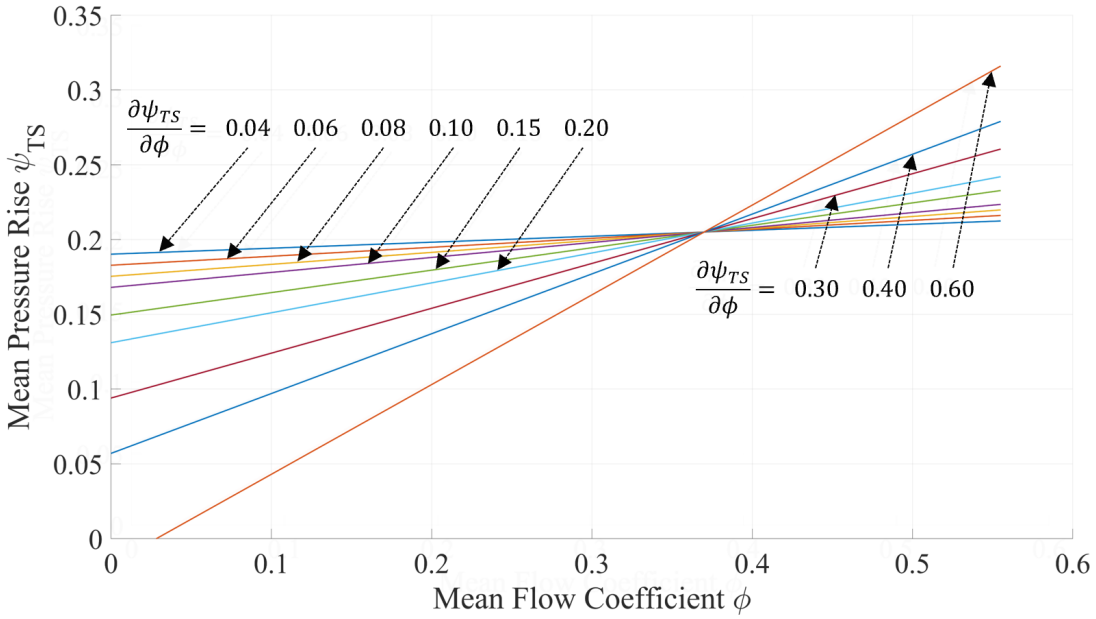

Figure 4.3: Constant slope pressure rise characteristics ($0.04 \leq \frac{\partial \psi_{TS}}{\partial \phi} \leq 0.6$) used in TBLOCK simulations.

4.3 Stall Inception Transients

We have not been able to capture fully developed rotating stall in the TBLOCK simulations, and we only consider the flow for times before reverse flow is detected. Using the procedure shown in Section 3.2, the SFC magnitude of the first harmonic of the axial velocity perturbations is plotted in Figure 4.4 for all the pressure rise slopes displayed in Figure 4.3. The cases are stacked on the SFC log-scale with the initial amplitude of -4 displaced by two units to display the change in time scale of stall inception for different slopes of the total-to-static pressure rise characteristic. For example, stall inception, defined in this chapter as the period between initial growth of perturbations up until reverse flow is detected, occurs over roughly 100 revolutions for $\frac{\partial \psi_{TS}}{\partial \phi} = 0.04$, whereas for $\frac{\partial \psi_{TS}}{\partial \phi} = 0.60$ inception occurs within 2 revolutions. Figure 4.4 shows the growth rate of the disturbances are proportional to the pressure rise slope. Increasing the constant slope yields increasing growth rates.

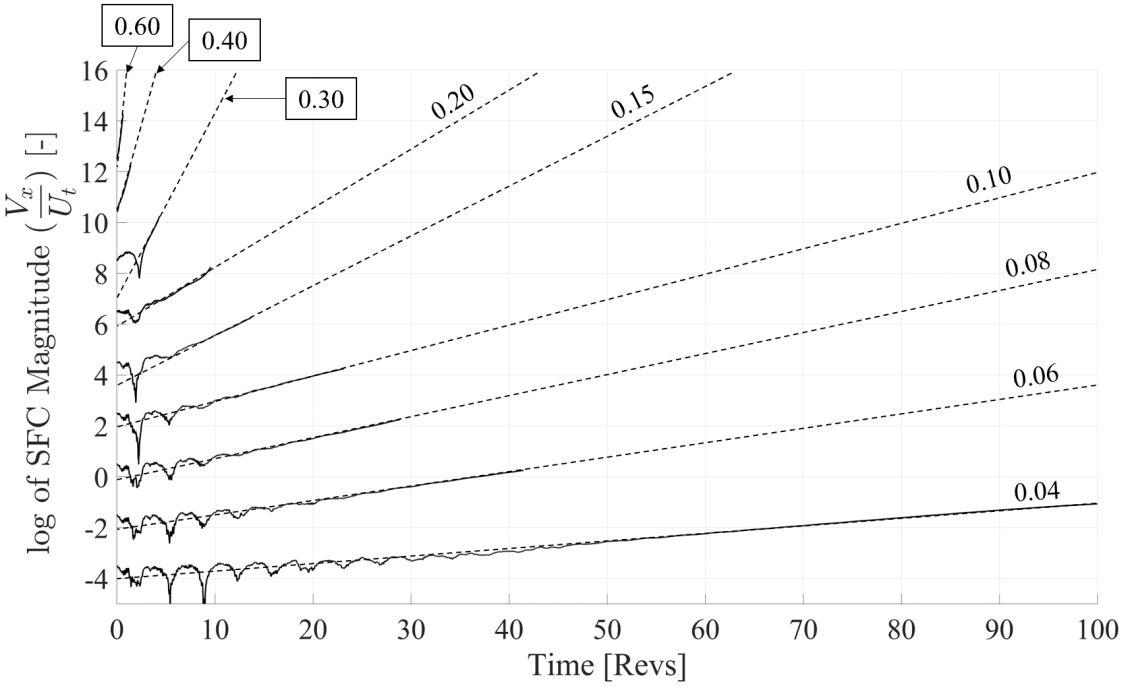

Figure 4.4: Magnitude of the first harmonic for TBLOCK cases showing an increase in growth rate for higher pressure rise slopes ($\frac{\partial \psi_{TS}}{\partial \phi}$ marked on each line).

The first six harmonics of the axial velocity traces are used to capture stall inception,

as no significant information is obtained from harmonics higher than $n = 6$. These six harmonics, along with the velocity traces for six equally spaced θ-locations, are plotted for $\frac{\partial \psi_{TS}}{\partial \phi} = 0.06$, 0.10, and 0.20 in Figures 4.6 to 4.8. Note that different scales for the x-axis are used on the different plots to better demonstrate the perturbation features. As in the linear analyses, there is a connection between the behavior of the perturbations and the slope of the mean total-to-static pressure rise. For shallower slopes (Figures 4.5 to 4.8), exponentially growing sinusoidal waves are seen in the axial velocity traces (the corresponding harmonics grow linearly in the log-scale). As stated in Chapter 2, this behavior of exponentially growing sinusoidal waves is indicative of modal inception. For a slope of 0.04 in Figure 4.5, the first harmonic is dominant, followed by the second, third, and so on, showing each harmonic growing at a different rate. As the slope is increased (Figure 4.6 to 4.8), however, the first harmonic becomes less dominant.

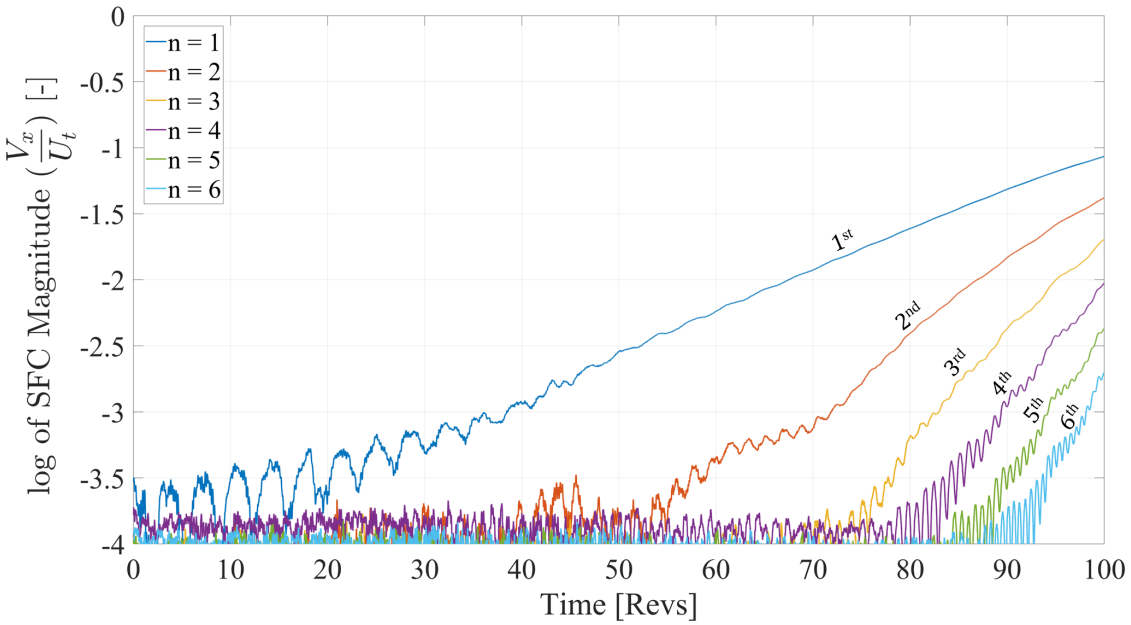

Figure 4.5: Magnitude of the SFC of axial velocity perturbations for $\frac{\partial \psi_{TS}}{\partial \phi} = 0.04$ showing higher growth rates for the higher harmonics.

For slopes of $\frac{\partial \psi_{TS}}{\partial \phi} = 0.30$ and 0.40, the SFC analysis was done on the pressure traces data (Figure 4.9 and 4.10), as the disturbances for these cases were clearer in the pressure signals.

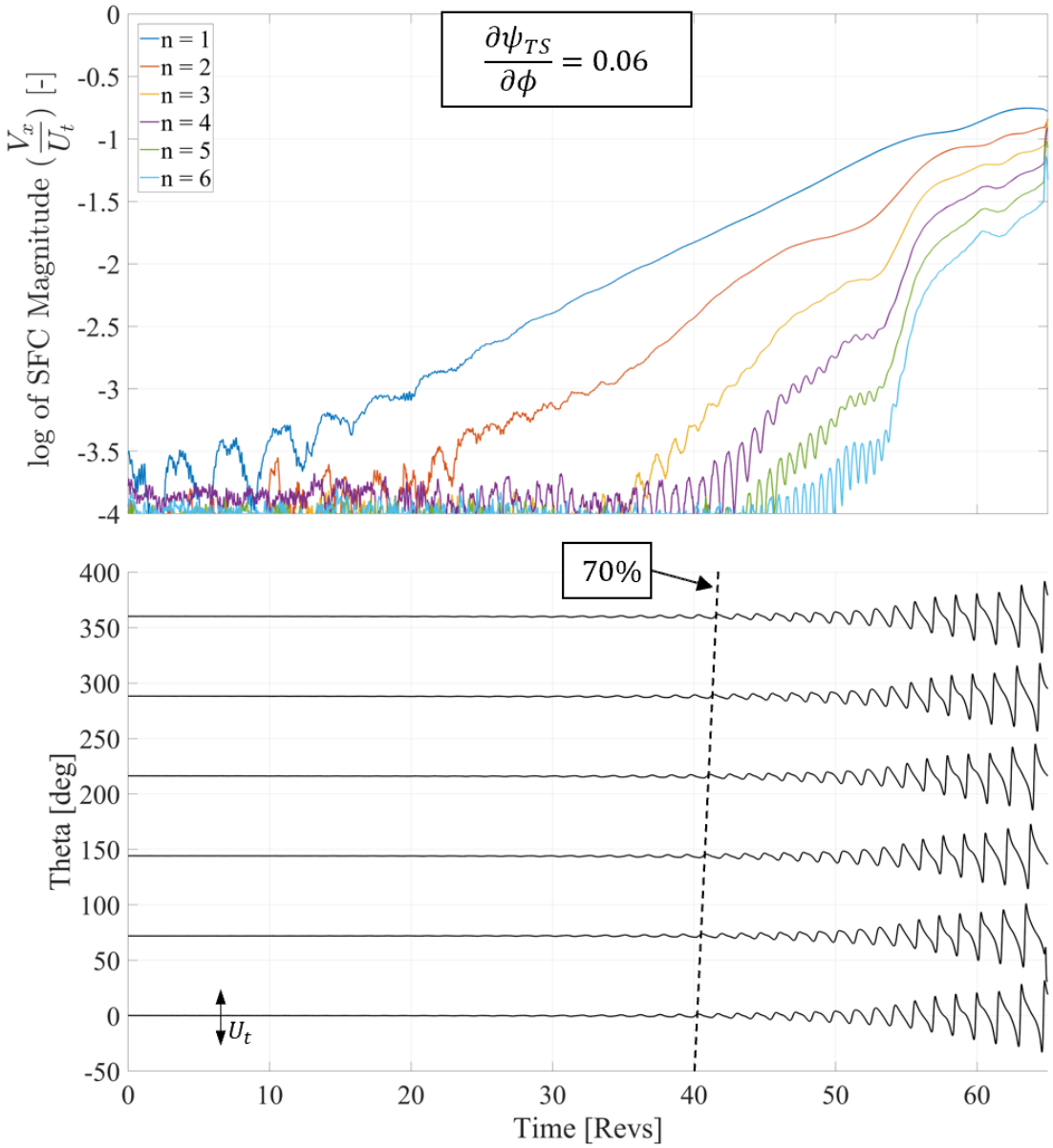

Figure 4.6: SFC and axial velocity traces showing modal inception for $\frac{\partial \psi_{TS}}{\partial \phi} = 0.06$ with propagation rate of 70% rotor speed.

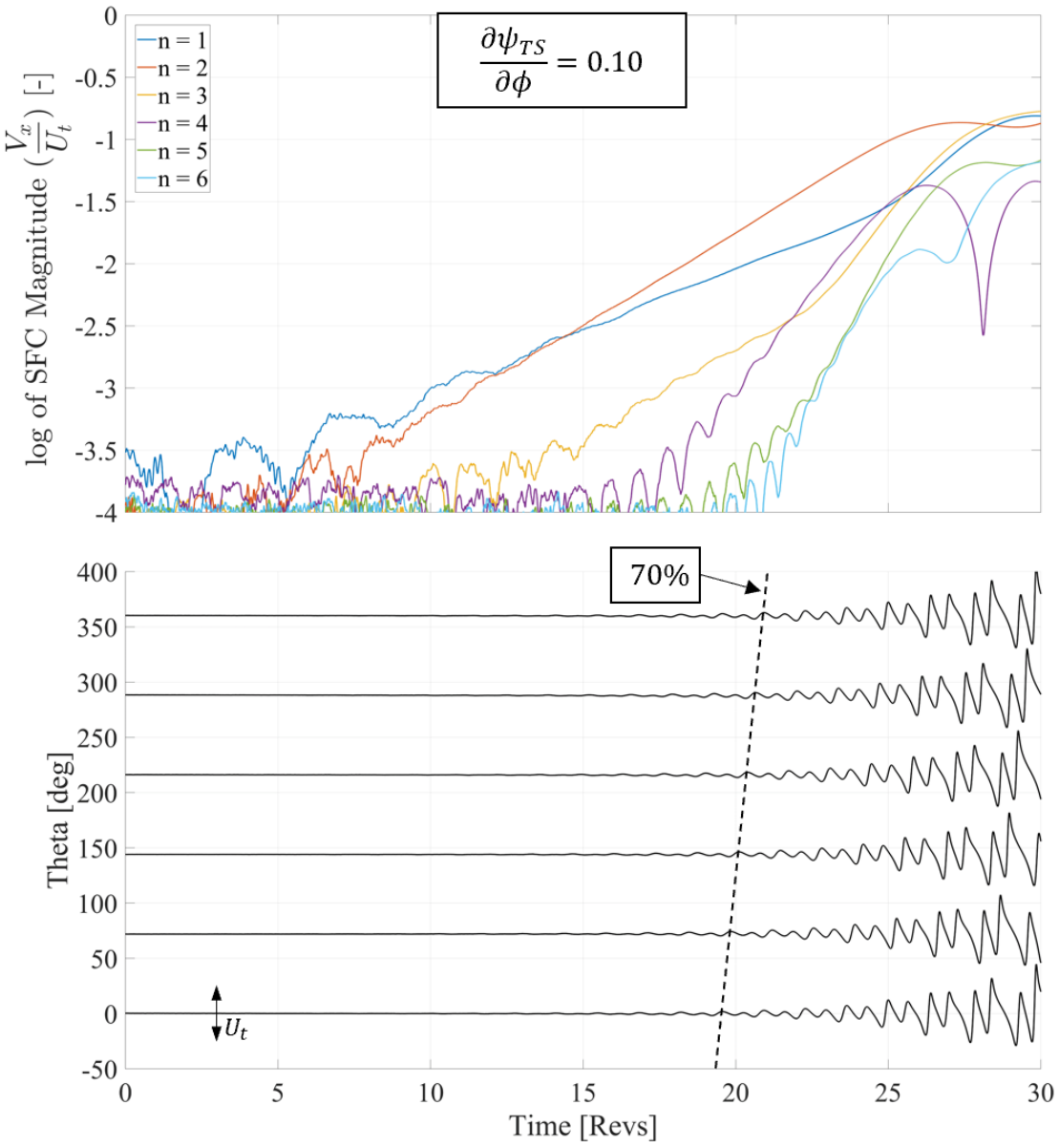

Figure 4.7: SFC and axial velocity traces showing modal inception for $\frac{\partial \psi_{TS}}{\partial \phi} = 0.10$ with propagation rate of 70% rotor speed.

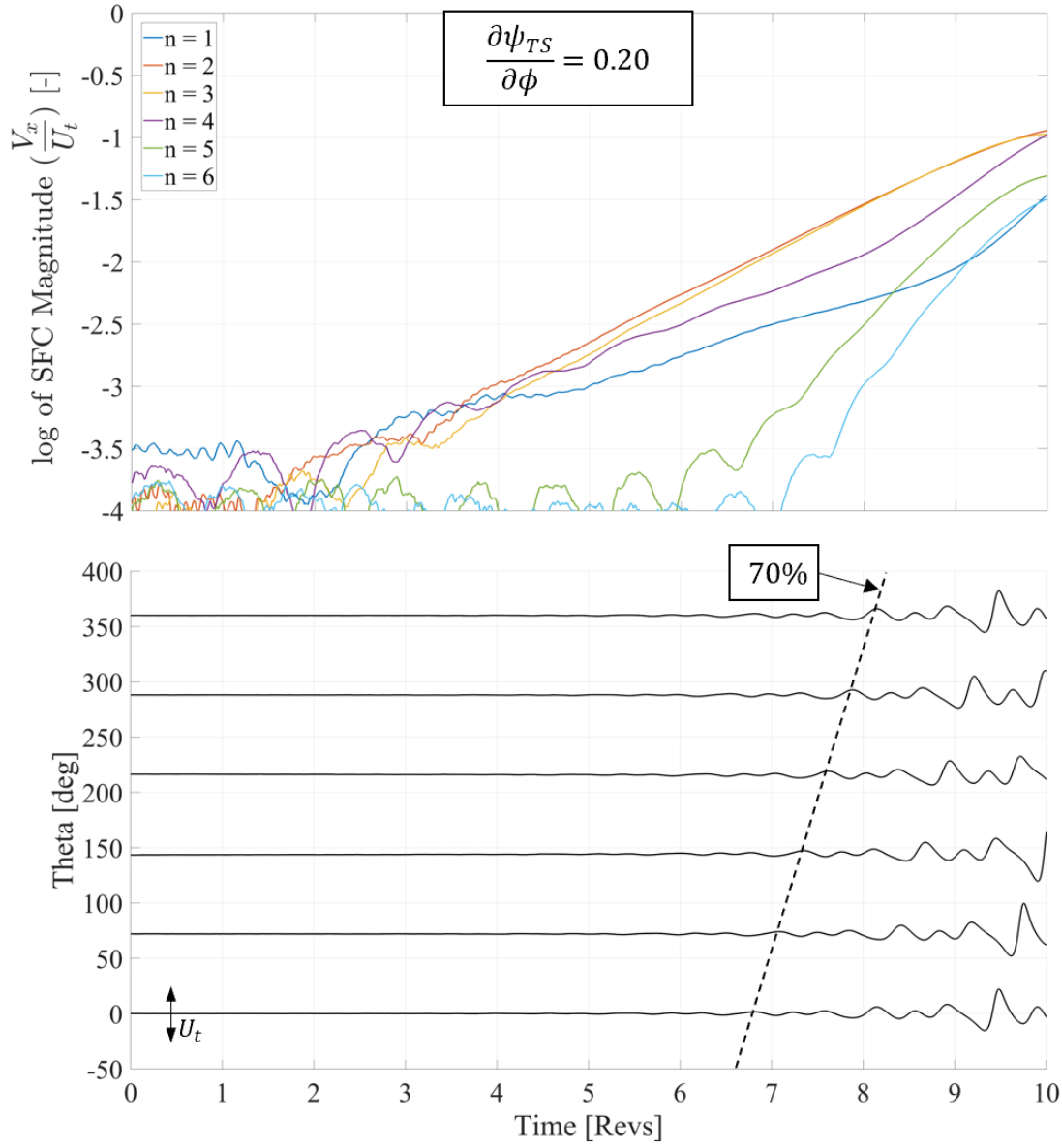

Figure 4.8: SFC and axial velocity traces showing second and third harmonics dominating in modal inception for $\frac{\partial \psi_{TS}}{\partial \phi} = 0.20$ with propagation rate of 70% rotor speed.

(The growth rate of the disturbance is equal in both axial velocity and static pressure traces, as shown in Figure B.2 of Appendix B)

The higher slope cases of Figures 4.9 and 4.10 exhibit different behaviors than found in Figures 4.5 to 4.8. For a mean pressure rise slope of 0.40, sinusoidal behavior is not seen. Also, unlike the shallow slope cases where higher harmonics exhibit higher growth rates, all harmonics grow at approximately the same rate, and spike-like disturbances are observed in the static pressure traces (Figures 4.9, 4.10). Further, these disturbances reach reverse flow an order of magnitude more rapidly than those observed in the shallower slope cases of Figures 4.5 to 4.8. Due to limitations of the computational model in the reverse flow, there is thus no data available after reverse flow is reached (see Figure 4.10). Also, unlike the modal cases, there is not an evident dominant harmonic during inception for the higher slope cases. Lastly, for $\frac{\partial \psi_{TS}}{\partial \phi} = 0.3$ a spike was observed developing on an exponentially growing sinusoidal perturbation (see Figure 4.9). Therefore, when looking at the behavior of the traces, the results for $\frac{\partial \psi_{TS}}{\partial \phi} = 0.3, 0.4$ and 0.6 indicate spike inception. The gradual shift from sinusoidal to spike disturbances observed in the TBLOCK calculations implies a transition regime between the two rotating stall inception routes.

4.3.1 Harmonic Growth Rates

We can obtain the growth rate of the harmonics by the slope of the SFC magnitude as a function of non-dimensional time, as in Section 3.2. In Figure 4.11 we compare the growth rate of the first harmonic as a function of pressure rise slope to the theoretical values from Spakovszky's analysis (Equation (2.15)). Three regimes are defined. For shallow slopes (0.04 to 0.20), the growth rates closely match the linear analysis. Between slopes of 0.20 and 0.40, the growth rates begin diverging from the linear model. For the highest slope cases, 0.40 and 0.60, the growth rates of the first harmonic are different than the linear theory by more than a factor of 3. In this regard we note that the theoretical model is based on the assumption of small amplitude perturbations. For spikes, however, this is not necessarily the case because

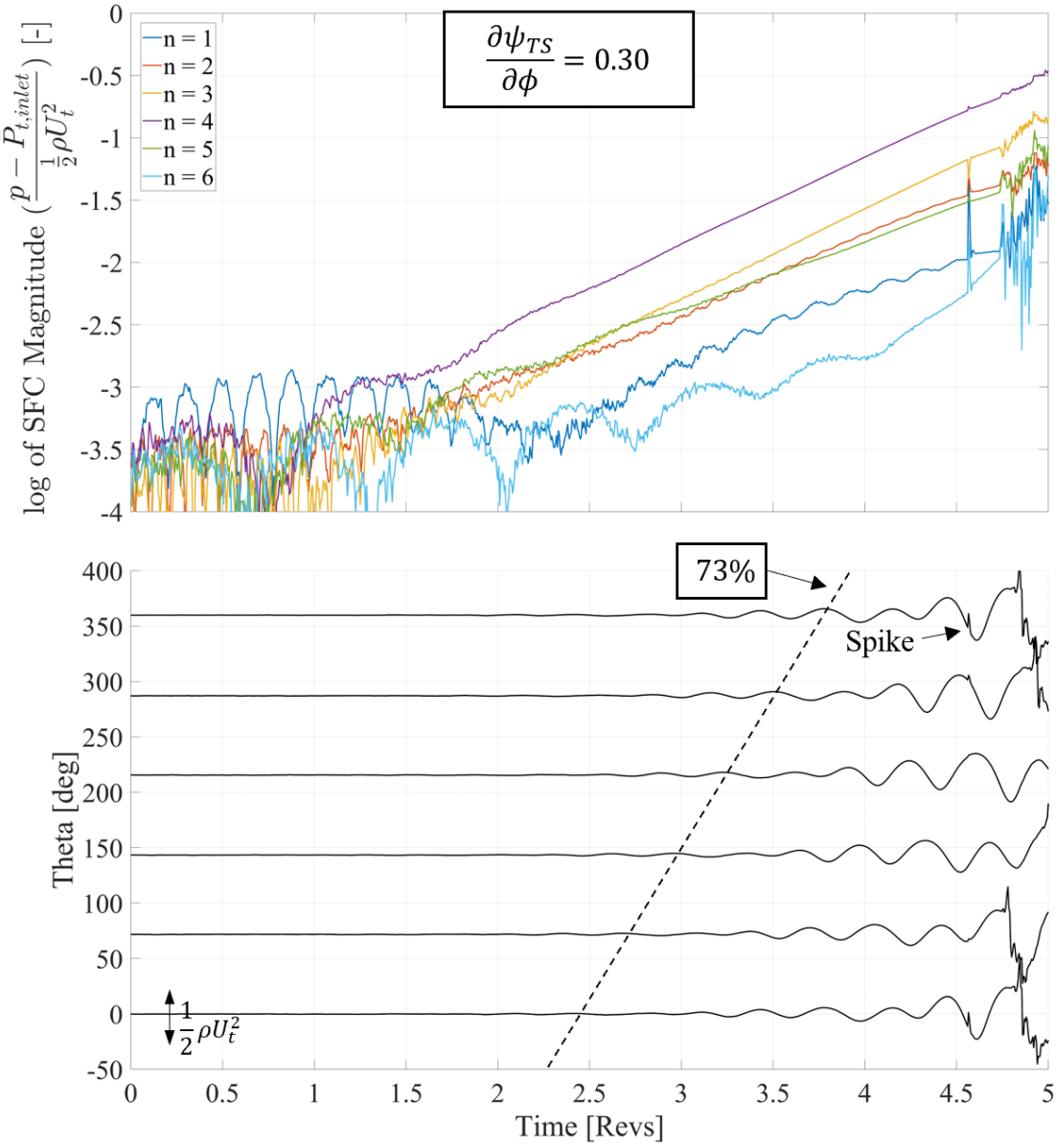

Figure 4.9: SFC and static pressure traces showing a spike developing over a fourth harmonic modal wave with propagation rate of 73% rotor speed for $\frac{\partial \psi_{TS}}{\partial \phi} = 0.30$.

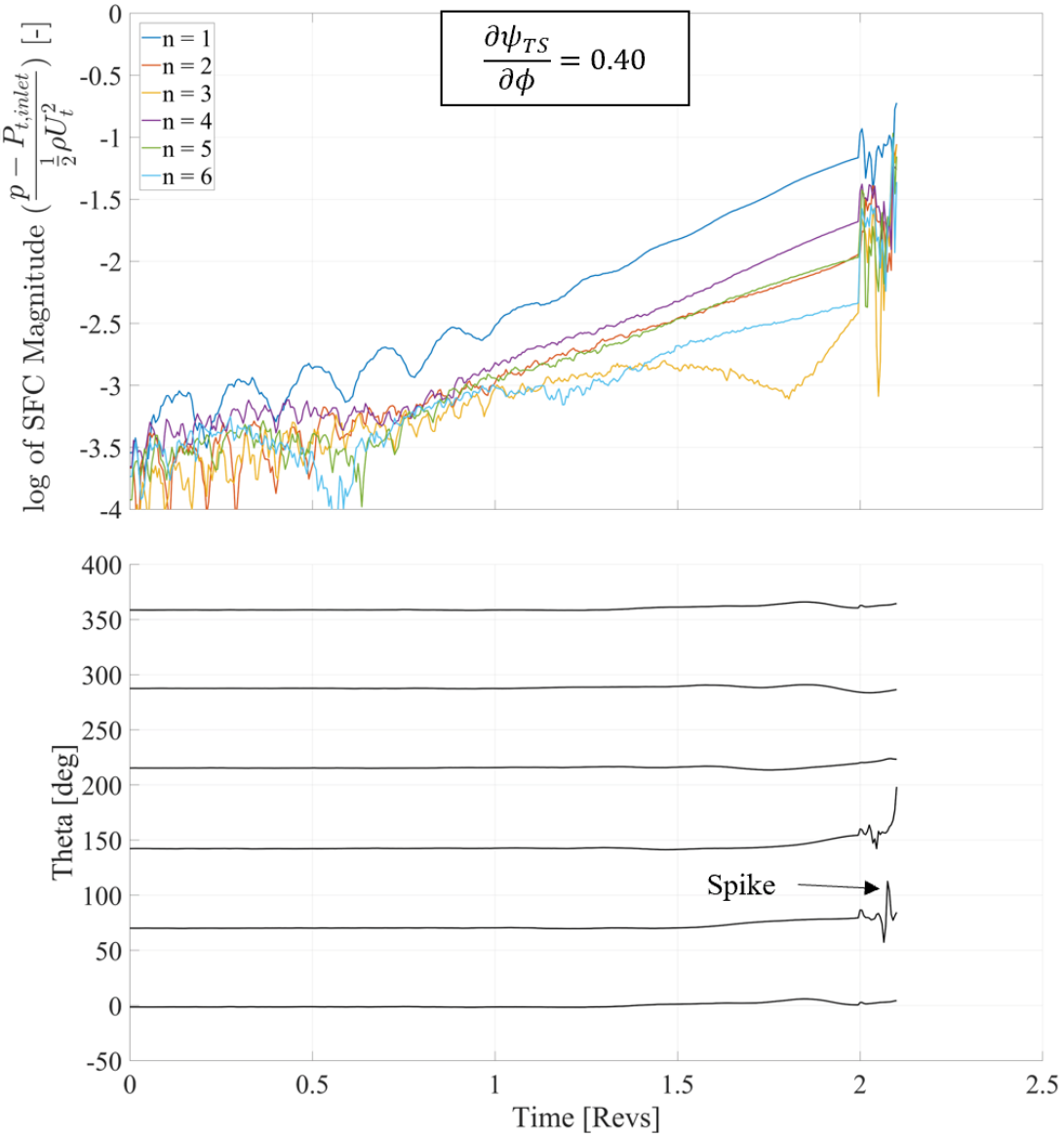

Figure 4.10: SFC and static pressure traces showing a developing spike for $\frac{\partial \psi_{TS}}{\partial \phi} = 0.40$.

the perturbations grow rapidly into reverse flow, which can lead to the bypassing of modal, sinusoidal behaviors. Therefore, an explanation can be that spike disturbances are large enough ($\frac{\Delta\phi}{\bar{\phi}} \approx 1$) so that the small perturbation assumption of the linear analyses do not apply.

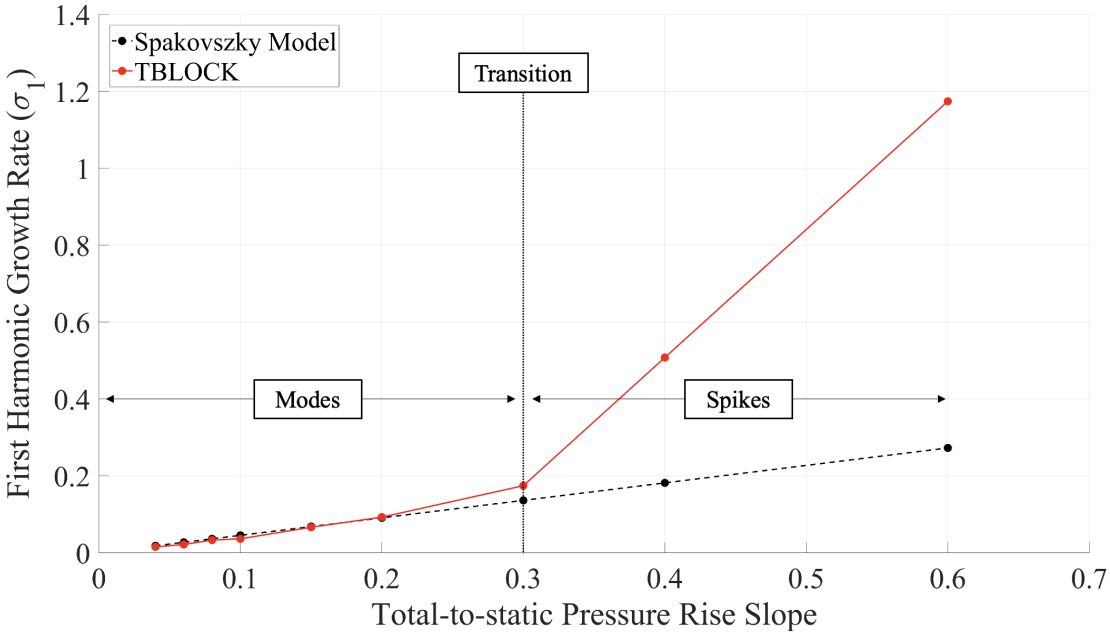

Figure 4.11: Non-dimensional growth rate of the first harmonic as a function of axisymmetric pressure rise slope.

Chapter 5

Summary and Conclusions

5.1 Primary Learnings

The main learnings in this thesis consist of (i) the quantification of the relationship between the slope of the axisymmetric total-to-static pressure rise characteristic and the rotating stall inception behavior, (ii) the demonstration that harmonic growth rates from linear analyses match results from actuator disk model for the modal regime, and (iii) the identification of the divergence from the linear analysis results in the spike inception regime. The parametric study, with constant slope pressure rise characteristics, showed regimes where either modes or spikes would appear. Based on these results, a slope-based criteria is proposed for determining the growth rate during rotating stall inception, in consistency with results obtained by Pullan [7][8]. The implication is thus a continuous, mode-spike transition. The following points apply for the parameters considered to date (Section 4.1.1).

- Modal inception is captured by both the linear analysis and the TBLOCK calculations. For this study, the modal inception regime is defined to be for total-to-static pressure rise slopes $\frac{\partial \psi_{TS}}{\partial \phi}$ below 0.2. In this regime the growth rates of the perturbations given by TBLOCK simulations closely match the two-dimensional linearized analysis, with exponentially growing sinusoidal waves observed. Also, the growth rate is proportional

to the product of the total-to-static pressure rise slope and the harmonic number n.

- Spike-like disturbances were observed when the slope of the total-to-static pressure rise curve with respect to flow coefficient were above 0.4. The growth rates of the spike disturbances measured from the actuator disk computations do not match those from the two-dimensional linear analysis, and the difference increases for higher slopes showing the effect of non-linearities in the spike inception process. An in-depth analysis of this behavior is outside the scope of this thesis.

- The continuum between modes and spikes is implied by the gradual transition from exponentially growing sinusoidal waves to spike-like disturbances observed from the TBLOCK calculations as the slope of the total-to-static pressure rise is increased.

5.2 Recommendations for Future Work

Several areas of improvements are needed to solidify the findings of this research. First, additional input parameter variations are essential to assess the generality of the results presented. It would be useful to study the effect of different angle variation magnitudes (RMS) or structures on the mode-spike transition, as the inlet flow angle variation remained unchanged for the analysis presented. Changing the blade passage inertia parameter (λ) and the incorporation of first order temporal lags in the loss parameter should also be considered to help understand what are the important factors in defining the mode-spike transition.

A sensitivity study on the TBLOCK temporal grid resolution (i.e number of explicit time steps per rotor revolution) should be carried out to test the consistency of the observed mode-spike transition with changes in computational settings. The development of modal and spike disturbances occur at different time scales, and higher temporal resolutions may be needed to capture spike inception accurately.

Finally, the source of disagreement between Stenning and Spakovszky analyses should be investigated (see Appendix A). For the modal cases, the computed rotation rates given

by TBLOCK were close to 70% of rotor speed, in agreement with values obtained from the Stenning formulation in Appendix A (see Figure A.2). Spakovszky's linear analysis, however, yields rotation rates of around 30% rotor speed [3]. The cause of the discrepancy is currently being addressed within the collaboration between the MIT Gas Turbine Laboratory and the University of Cambridge Whittle Lab.

Appendix A

Stenning Small Perturbation Analysis

Consider the two – dimensional flow in Figure A.1 , with an isolated rotor bounded by upstream and downstream infinite length ducts. Stations 1 and 2 are at the upstream and downstream sides of the cascade, with $x = 0$ at the rotor leading edge. The flow upstream is incompressible, irrotational, and inviscid. The mean or "background" flow enters the blade row with zero inlet swirl ($\alpha_1 = 0$) and leaves the blade row at a constant relative exit flow angle β_2. Upstream of the cascade, we consider the development of small perturbations and

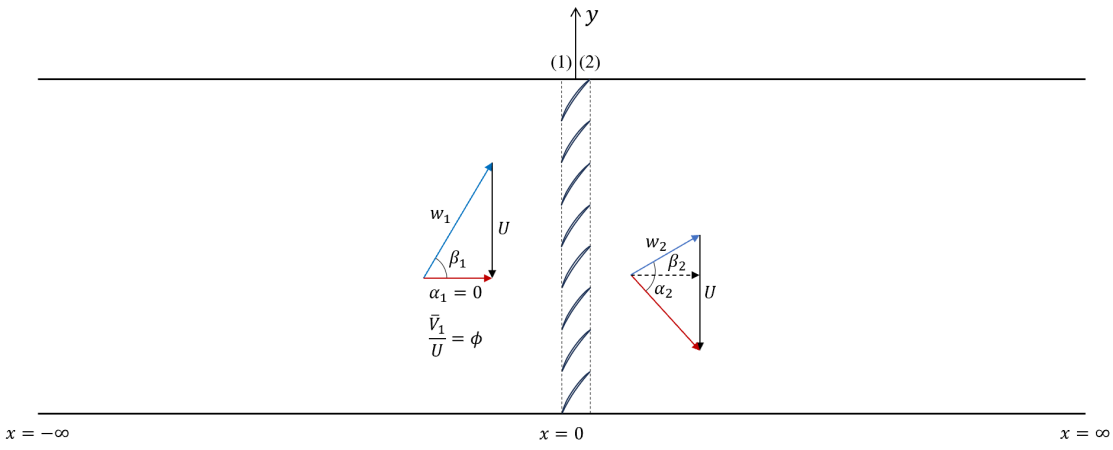

Figure A.1: Two - dimensional isolated rotor model as presented in Stenning's analysis.

describe the flow variables as

$$w_x = \bar{w}_x + u, \tag{A.1}$$

$$w_y = \bar{w}_y + v, \tag{A.2}$$

$$p = \bar{p} + \delta p, \tag{A.3}$$

where w_x and w_y are the x and y components of the relative velocity w, and p is the static pressure. Far upstream of the rotor ($x \to -\infty$) perturbations are negligible, and the flow is steady and uniform:

$$w_x = \bar{w}_x, \tag{A.4}$$

$$w_y = \bar{w}_y, \tag{A.5}$$

$$p = \bar{p}. \tag{A.6}$$

The quantities u, v, and δp are the perturbations of the axial velocity, tangential velocity, and static pressure. For irrotational flow, we can define a velocity perturbation potential, φ, for the upstream flow field such that

$$u = \frac{\partial \varphi}{\partial x}, \tag{A.7}$$

$$v = \frac{\partial \varphi}{\partial y}. \tag{A.8}$$

The continuity equation is

$$\frac{\partial u}{\partial x} + \frac{\partial v}{\partial y} = 0, \tag{A.9}$$

and the equation for the potential is Laplace's Equation:

$$\frac{\partial^2 \varphi}{\partial x^2} + \frac{\partial^2 \varphi}{\partial y^2} = 0. \tag{A.10}$$

A solution for the perturbation potential in Cartesian coordinates is

$$\varphi(x, y, s, t) = \sum_{n=1}^{\infty} A_n e^{s\bar{t}} e^{\frac{n}{R}(x+iy)}, \tag{A.11}$$

where $s = \sigma_n - i\omega_n$ are the eigenvalues of the isolated rotor system, $\bar{t} = \frac{Ut}{R}$ the non-dimensional time using the rotor speed U and radius R, and A_n the amplitude of the n-th component of the Fourier series.

For the n-th harmonic, the eigenvalues σ_n and ω_n correspond to the non-dimensional growth and rotation rates, respectively. The linearized x-momentum equation gives a relation between the velocity and static pressure perturbations :

$$\left(\frac{\partial \varphi}{\partial t}\right)_1 + \bar{w}_x \left(\frac{\partial \varphi}{\partial x}\right)_1 + \bar{w}_y \left(\frac{\partial \varphi}{\partial y}\right)_1 = -\frac{\delta p_1}{\rho}. \tag{A.12}$$

We define a pressure rise coefficient such that

$$c_p = f(\tan \beta_1) = \frac{p_2 - p_1}{\frac{1}{2}\rho w_1^2}, \tag{A.13}$$

with

$$\tan \beta_1 = \left(\frac{w_y}{w_x}\right)_1. \tag{A.14}$$

Assuming that the perturbations are small such that $u, v << \bar{w}_x, \bar{w}_y$ and $\delta p << \frac{1}{2}\rho w^2$, we linearize Equation (A.13) as the average value plus perturbation in upstream flow angle:

$$c_p = \bar{c}_p + \frac{\partial \bar{c}_p}{\partial \tan \bar{\beta}_1} \delta (\tan \beta_1). \tag{A.15}$$

In Equation (A.15):

$$\delta (\tan \beta_1) = \frac{\bar{w}_x v_1 - \bar{w}_y u_1}{\bar{w}_x^2}. \tag{A.16}$$

Using Equations (A.13) and (A.15) gives the following relation describing the static pressure

change across the rotor:

$$\frac{\delta p_2}{\rho} - \frac{\delta p_1}{\rho} = \bar{c}_p \left(\bar{w}_x u_1 + \bar{w}_y v_1\right) + \frac{1}{2}\bar{w}_1^2 \frac{\partial \bar{c}_p}{\partial \tan \bar{\beta}_1} \delta \left(\tan \beta_1\right). \tag{A.17}$$

There is zero upstream swirl for the mean flow, so the mean flow coefficient ϕ is a function of inlet flow angle only

$$\phi = \frac{\bar{w}_x}{U} = -\frac{\bar{w}_x}{\bar{w}_y} = -\frac{1}{\tan \bar{\beta}_1}. \tag{A.18}$$

Stenning assumed that $\delta p_2 << \delta p_1$. If so, Equations (A.17) and (A.11) can be substituted in Equation (A.12) to give the real and imaginary parts of the eigenvalue

$$\text{Real: } s_r = n\left(-(1-\bar{c}_p)\phi + \frac{1}{2\cos^2 \bar{\beta}_1} \frac{\partial \bar{c}_p}{\partial \tan \bar{\beta}_1}\right), \tag{A.19}$$

$$\text{Imaginary: } s_i = n\left(-(1-\bar{c}_p) - \frac{\phi}{2\cos^2 \bar{\beta}_1} \frac{\partial \bar{c}_p}{\partial \tan \bar{\beta}_1}\right). \tag{A.20}$$

It is convenient to express Equations (A.19) and (A.20) in terms of the mean total-to-static pressure rise characteristic ψ_{TS}:

$$\psi_{TS} = f(\phi) = \frac{p_2 - p_{t1}}{\rho U^2}. \tag{A.21}$$

The mean pressure rise $\bar{c}_p$ and total-to-static characteristic ψ_{TS} are connected through the relation

$$\bar{c}_p = \frac{2\psi_{TS} + \phi^2}{1 + \phi^2}. \tag{A.22}$$

The derivative of the mean pressure rise coefficient with respect to the tangent of $\bar{\beta}_1$ can be expressed using the derivative of $\bar{c}_p$ with respect to the flow coefficient ϕ

$$\frac{\partial \bar{c}_p}{\partial \tan \bar{\beta}_1} = \frac{1}{\tan^2 \bar{\beta}_1} \frac{\partial \bar{c}_p}{\partial \phi}. \tag{A.23}$$

Therefore, from Equations (A.22) and (A.23)

$$\frac{\partial \bar{c}_p}{\partial \tan \bar{\beta}_1} = 2\cos^2 \bar{\beta}_1 \left(\frac{\partial \psi_{TS}}{\partial \phi} - \phi \sin^2 \bar{\beta}_1 \left(\psi_{TS} - 1 \right) \right). \tag{A.24}$$

The eigenvalue solutions are given below as a function of the total-to-static pressure rise coefficient, ψ_{TS}, and the mean flow coefficient ϕ in Equations (A.25) and (A.26). To express s_i in the absolute frame, we add the the non-dimensional rotor speed to Equation (A.20).

$$s_r = n \left(\frac{\partial \psi_{TS}}{\partial \phi} \right), \tag{A.25}$$

$$s_i = n \left(2\psi_{TS} - \frac{\partial \psi_{TS}}{\partial \phi} \phi \right). \tag{A.26}$$

Equations (A.25) and (A.26) were obtained assuming negligible downstream pressure perturbations. To include the downstream effects, an expression for δp_2 in Equation (A.17) is also needed. For constant exit flow angle β_2, the downstream pressure perturbations are given by

$$\frac{\partial u_1}{\partial t} = -\frac{1}{\rho} \frac{\partial \delta p_2}{\partial x}. \tag{A.27}$$

The static pressure perturbations are also a solution of Laplace's equation and δp_2 can be written as

$$\delta p_2 = \sum_{n=1}^{\infty} B e^{s\bar{t}} e^{\frac{n}{R}(x+y)}. \tag{A.28}$$

Using Equations (A.28) and (A.11) in the downstream pressure condition, re-evaluating Equation (A.17), and solving for s, the growth and rotation rates of the n-th harmonic (including downstream perturbations) become

$$\frac{\sigma_{n,Stenning}}{n} = \frac{1}{2} \left(\frac{\partial \psi_{TS}}{\partial \phi} \right), \tag{A.29}$$

$$\frac{\omega_{n,Stenning}}{n} = \frac{1}{2} \left(2\psi_{TS} - \frac{\partial \psi_{TS}}{\partial \phi} \phi + 1 \right). \tag{A.30}$$

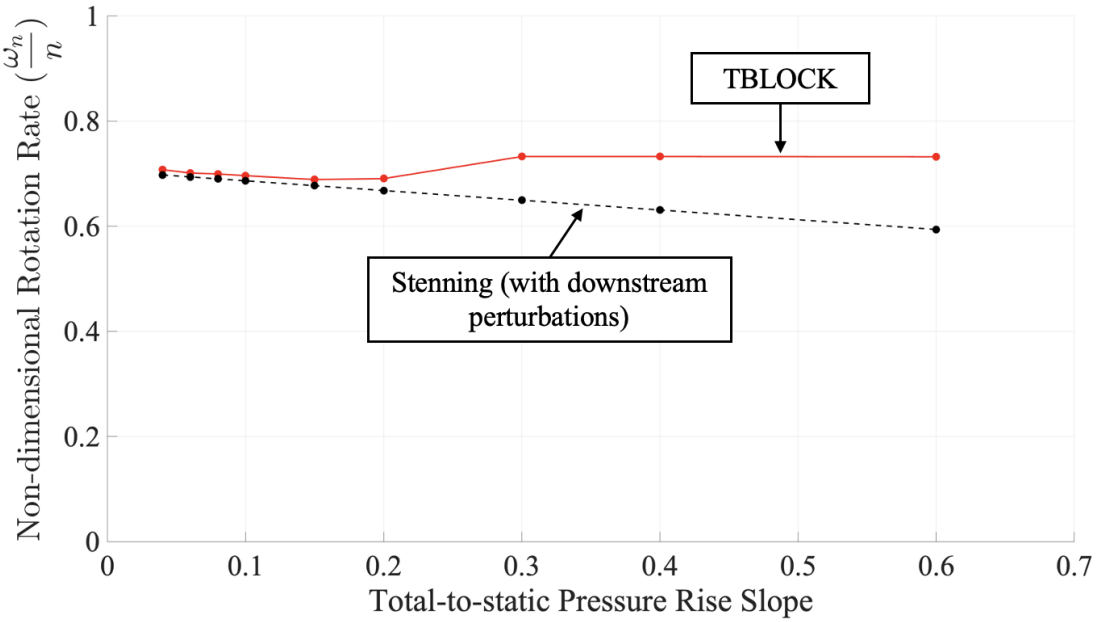

Figure A.2: Analytical non-dimensional rotation rates compared with TBLOCK simulation results for different total-to-static pressure rise slopes.

It is noted that, by neglecting the blade passage inertia term λ, Equation (2.15) for the growth rates from Spakovszky's analysis reduces to Equation (A.29). However, the ideal pressure rise term present in Equation (2.16) does not appear in Equation (A.30) since, for Stenning's analysis, there is no mention or consideration of the pressure loss across the blade row. Neglecting the inertia term λ, Spakovszky's solution for the disturbance rotation rate of an isolated rotor becomes

$$\frac{\omega_{n,Spakovszky}}{n} = \frac{1}{2}\left(2\psi_{TS}^{I} - \phi\frac{\partial\psi_{TS}}{\partial\phi}\right) \tag{A.31}$$

The measured disturbance rotation rates from the TBLOCK cases and the Stenning analyses are plotted in Figure A.2. The two agree well for pressure rise slopes below 0.2. This was first pointed out by Grimshaw [8] (in communications between the Whittle Lab and the Gas Turbine Lab). For $\frac{\partial\psi_{TS}}{\partial\phi} > 0.2$, the TBLOCK rotation rates diverge from the Stenning analytical solution, with behavior similar to that seen in Figure 4.11.

Appendix B

TBLOCK Actuator Disk Solver

B.1 Compressible Flow Routine

Across the actuator disk, mass, radial momentum, and rothalpy is conserved, so the average quantities become

$$\overline{\rho V_x} = (\rho V_x)_1 = (\rho V_x)_2, \tag{B.1}$$

$$\overline{V}_r = V_{r_1} = V_{r_2}, \tag{B.2}$$

$$\overline{T}_{t_{rel}} = (T_{t_{rel}})_1 = (T_{t_{rel}})_2, \tag{B.3}$$

where $T_{t_{rel}}$ is the relative stagnation temperature. On the upstream side, the entropy s_1 and tangential velocity V_{θ_1} are extrapolated from the Euler equation solutions. An iterative problem for upstream density ρ_1 is set to converge the upstream side quantities. Starting with an initial guess for density ρ_{g}, the axial velocity is

$$V_{x_1} = \frac{\overline{\rho V_x}}{\rho_{\mathrm{g}}}. \tag{B.4}$$

From velocity triangles, the relative tangential velocity is

$$w_{\theta_1} = V_{\theta_1} - \Omega r, \tag{B.5}$$

where r is the local radius and Ω is the specified rotational speed of the disk. The static temperature is computed from

$$T_1 = \overline{T}_{t_{rel}} - \frac{V_{x_1}^2 + w_{\theta_1}^2 + \overline{V}_r^2}{2C_p}. \tag{B.6}$$

For Equation (B.6), C_p is the heat capacity of air at room temperature. Using a reference temperature T_{ref}, reference pressure P_{ref}, and the ideal gas constant R_{air}, the static pressure is given from

$$\frac{P_1}{P_{\text{ref}}} = \exp \frac{C_p \log\left(\frac{T_1}{T_{\text{ref}}}\right) - s_1}{R_{\text{air}}}. \tag{B.7}$$

The upstream density is re-evaluated using the ideal gas law:

$$\rho_1 = \frac{P_1}{R_{\text{air}} T_1}. \tag{B.8}$$

If the difference between ρ_1 and ρ_{g} is not within the accepted tolerance, the current ρ_1 is taken as the next guess, and Equations (B.4) to (B.8) are solved again. This process is repeated until satisfactory convergence is reached. Then, the upstream relative flow angle β_1 is computed with

$$\beta_1 = \tan^{-1}\left(\frac{w_{\theta_1}}{V_{x_1}}\right) + \Delta\beta_1. \tag{B.9}$$

where $\Delta\beta_1$ is an input local disturbance rotating at disk frequency Ω and varying across the circumference. Using the computed local β_1, the loss is interpolated from the input $\zeta = f(\beta_1)$ curve. The downstream entropy is thus given by

$$s_2 = s_1 + \zeta \frac{w_1^2}{2T_1}. \tag{B.10}$$

With s_2, the downstream pressure, temperature, and velocities are found using the same iterative problem for density as in the upstream side. After ρ_2 is solved, the downstream static pressure is modified by an unsteady term representing the acceleration in the blade passage defined as

$$\Delta P_{\text{inertia}} = -\left(\lambda \rho U^2\right) \frac{\partial \phi}{\partial \tau}, \tag{B.11}$$

where λ is the inertia parameter as defined in Equation (2.1). The derivative $\frac{\partial \phi}{\partial \tau}$ is estimated using axial velocities from previous time steps. The procedure presented in this section is evaluated for all the circumferential and radial nodes of the actuator disk.

B.2 Mesh Geometry

In this work we use a high hub-to-tip ratio mesh ($\frac{r_{\text{tip}}}{r_{\text{hub}}} = 0.9999$) with 7 radial nodes and 101 circumferential (or tangential) nodes. The 7 radial nodes give a cell height approximately half of the compressor blade pitch[1] and set the radial and circumferential extents to be roughly equal. The geometry was constructed by taking an annular disk of $\frac{r_{\text{tip}}}{r_{\text{hub}}} = 0.75$ and converting it into a quasi two-dimensional cascade of $\frac{r_{\text{tip}}}{r_{\text{hub}}} = 0.9999$, as in Figure B.1.

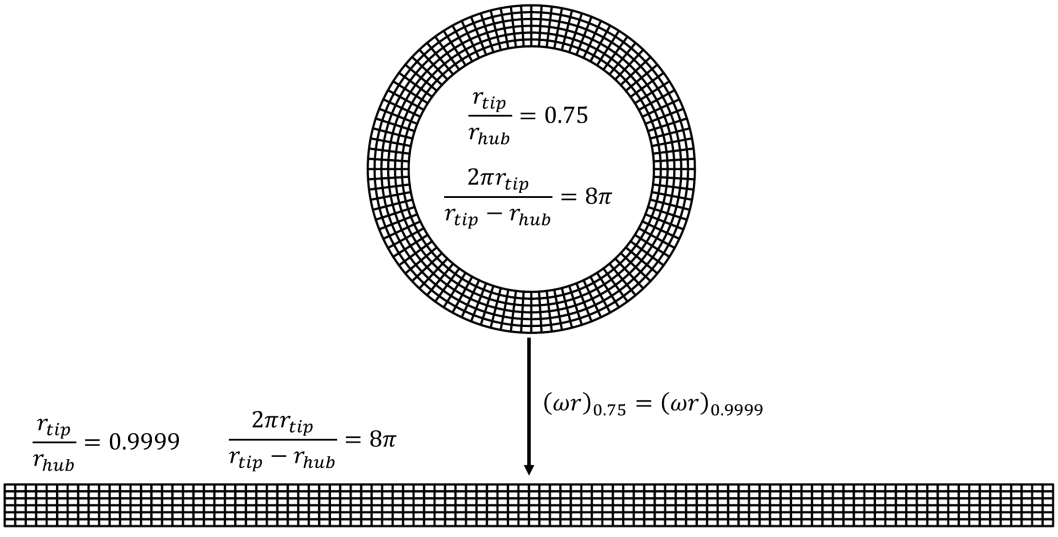

Figure B.1: Actuator disk mesh for quasi two-dimensional calculations.

[1] Taken from compressor rig measurements at the University of Cambridge [7]

The radial span, circumference, and rotational speed were conserved between the annular and high hub-to-tip ratio geometries such that the resulting quasi two-dimensional geometry has an equivalent fluid inertia. Three-dimensional variations in pressure and flow coefficient are suppressed for the high hub-to-tip geometry to examine stall inception in a quasi two-dimensional framework and compare with a linear model.

B.3 Pressure and Velocity Perturbations

From the TBLOCK simulations, we can obtain data on pressure and velocity signals at all the circumferential points of the actuator disk tip region. Therefore, we can apply the spatial Fourier decomposition from Section 3.2 to both the pressure and velocity disturbances. Figure B.2 shows an example, where the first six harmonics for the $\frac{\partial \psi_{TS}}{\partial \phi} = 0.06$ case (see Chapter 4) are plotted for the SFC of the pressure and axial velocity disturbances. While a higher degree of noise is observed in the pressure SFC, the corresponding harmonics have identical growth rates in both pressure and axial velocity traces, Therefore, we can obtain the same information when applying the SFC analysis to either one.

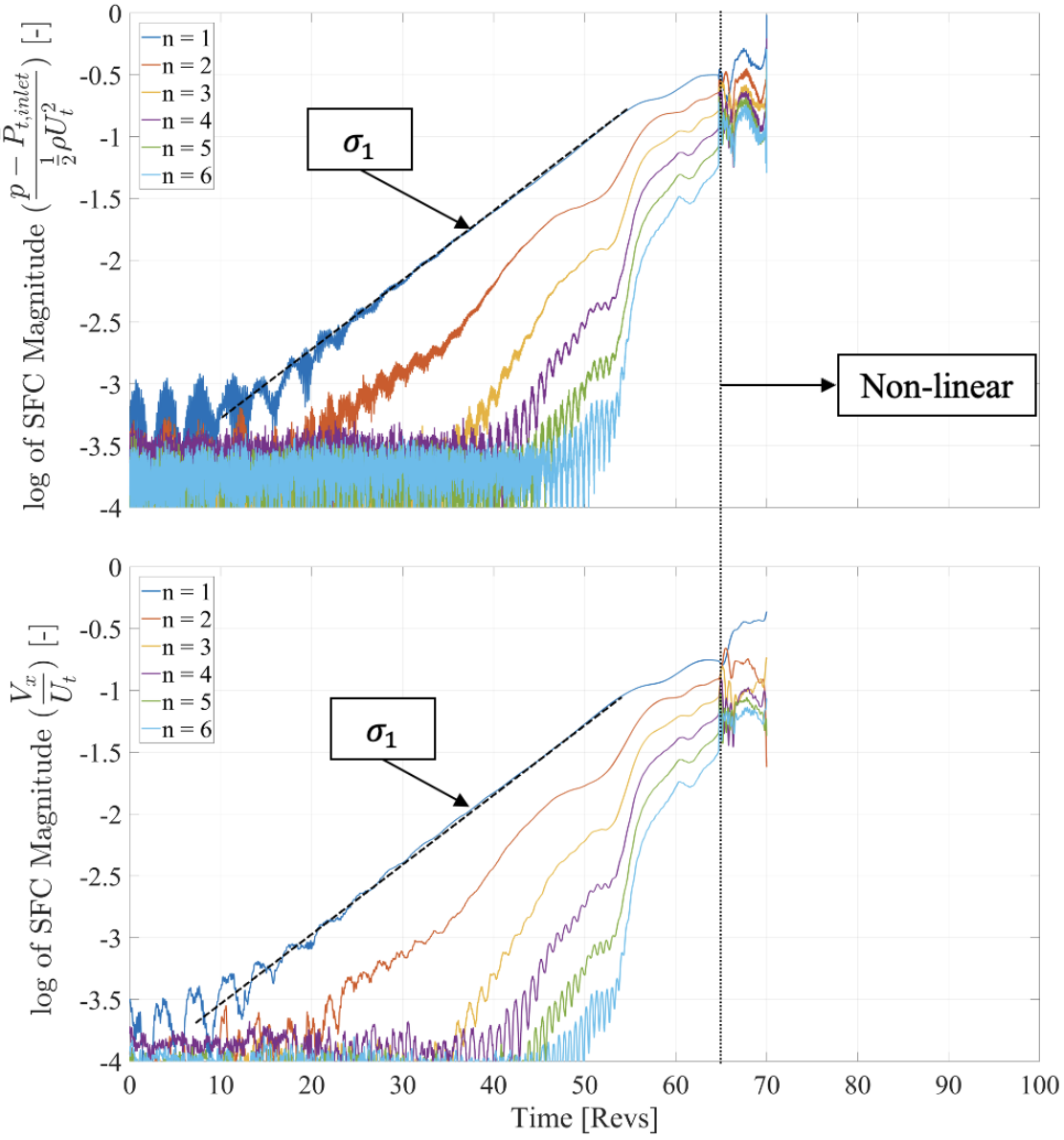

Figure B.2: Magnitude of the SFC of pressure and axial velocity perturbations for $\frac{\partial \psi_{TS}}{\partial \phi} = 0.06$. After 65 revolutions, the harmonics behave in a non-linear manner due to the large amplitudes reaching reverse flow, and the simulation stops shortly after.

Appendix C

Isolated Rotor Eigenvalues for Moore-Greitzer Pressure Rise Curve

For the Moore-Greitzer formulation in Equation (2.17), the slope of the mean total-to-static pressure rise can be computed directly by taking the derivative of the cubic ψ_{TS} with respect to ϕ. Applying Equation (2.15) with $\lambda = 0$, the growth rates for the first four harmonics are plotted in Figure C.1 along with the slope of the mean cubic ψ_{TS}. In Figure C.2, the rotation rate ω_1 is also plotted using the above parameters for Equation (2.16). This is shown as an example for the computation of the eigenvalues for a given axisymmetric curve.

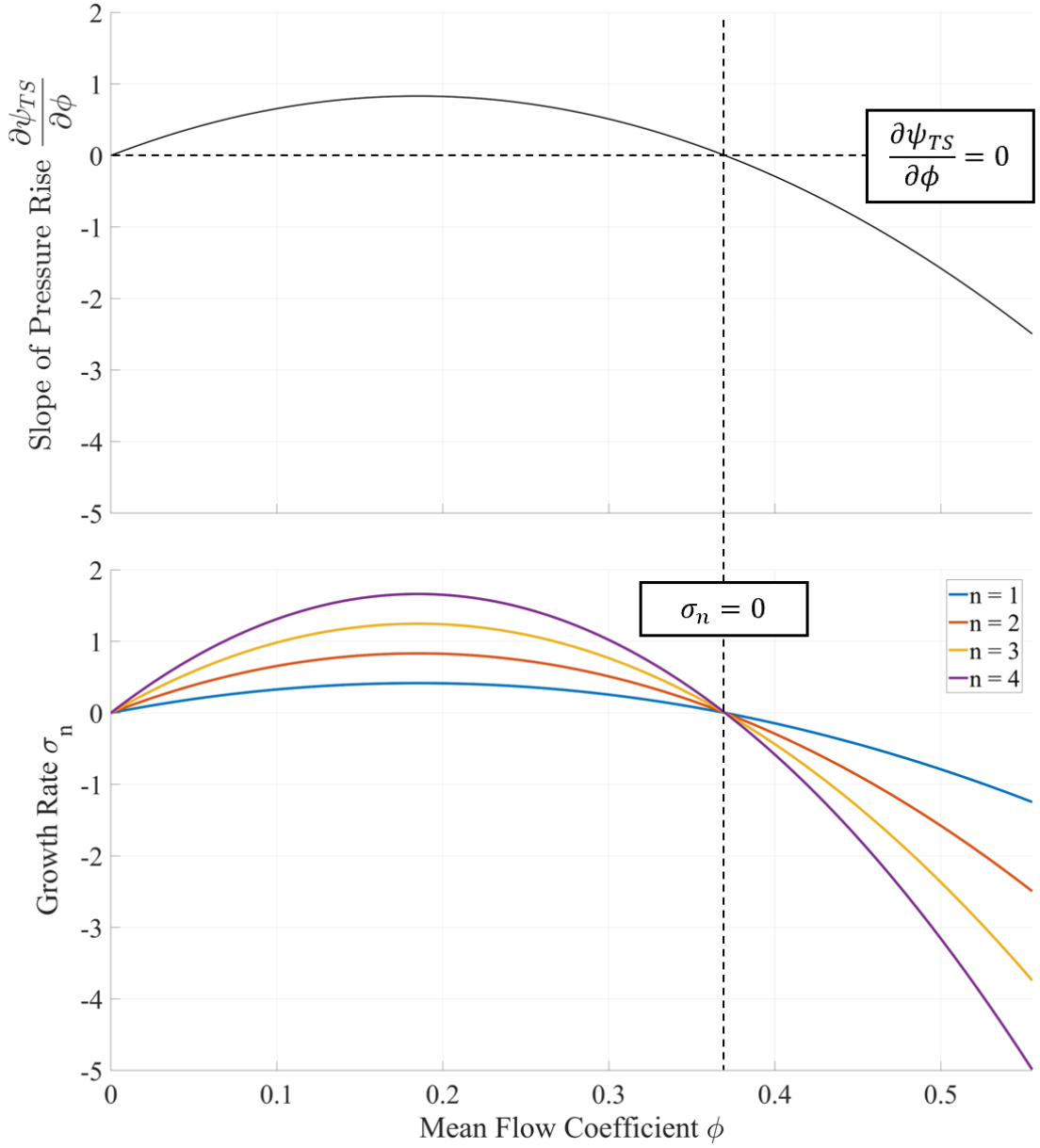

Figure C.1: Non-dimensional growth rates of the first 4 pre-stall harmonics for Moore-Greitzer cubic characteristic based on Spakovszky's isolated rotor analysis.

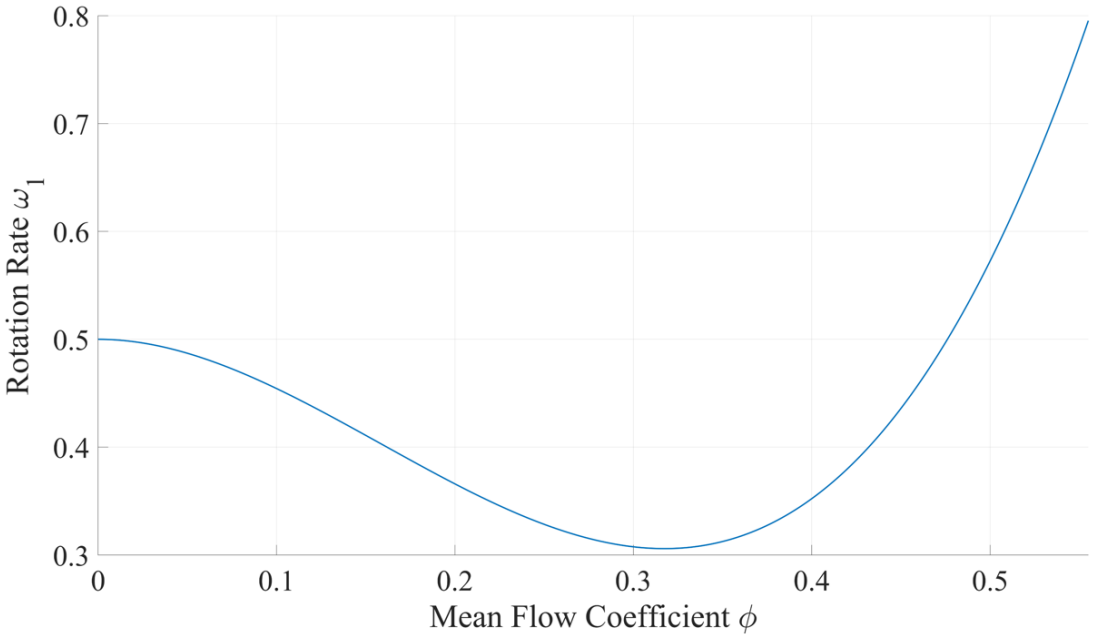

Figure C.2: Non-dimensional rotation rate for Moore-Greitzer cubic characteristic based on Spakovszky's isolated rotor analysis.

Bibliography

[1] I.J. Day, "Stall, Surge, and 75 Years of Research," *ASME Journal of Turbomachinery*, vol. 138, no. 1, 2016. DOI: 10.1115/1.4031473.

[2] A.H. Stenning, "Rotating Stall and Surge," *ASME Journal of Fluids Engineering*, vol. 102, no. 1, pp. 14–20, 1980. DOI: 10.1115/1.3240618.

[3] Z. Spakovszky, "Applications of Axial and Radial Compressor Dynamic System Modeling," Ph.D. Dissertation, Massachusetts Institute of Technology, Cambridge, MA, 2001.

[4] I.J. Day, "Stall Inception in Axial Flow Compressors," *ASME Journal of Turbomachinery*, vol. 115, pp. 1–9, 1993. DOI: 10.1115/1.2929209.

[5] T.R. Camp and I.J. Day, "A Study of Spike and Modal Stall Phenomena in a Low-Speed Axial Compressor," *ASME Journal of Turbomachinery*, vol. 120, no. 3, pp. 393–401, 1998. DOI: 10.1115/1.2841730.

[6] G. Pullan et al., "Origins and Structure of Spike-Type Rotating Stall," *ASME Journal of Turbomachinery*, vol. 137, no. 5, 2015. DOI: 10.1115/1.4028494.

[7] G. Pullan et al., "A Unified Framework for Compressor Stall Inception," MHI Turbomachinery Workshop, Takasago, Japan, Apr. 2023.

[8] G. Pullan et al., "Compressor Stall Inception," University of Cambridge - MIT, MHI Report Meeting, Sep. 2022.

[9] H.W. Emmons et al., "Compressor Surge and Stall Propagation," *ASME Journal of Fluids Engineering*, vol. 77, no. 4, 1955. DOI: 10.1115/1.4014389.

[10] J. Dunham, "Non-Axisymmetric Flows in Axial Compressors," Insititution of Mechanical Engineers, Mechanical Engineering Science Monograph No. 3, Oct. 1965.

[11] F.K. Moore, "A Theory of Rotating Stall of Multistage Axial Compressors: Part I — Small Disturbances," *ASME Journal of Engineering for Gas Turbines and Power*, vol. 106, no. 2, pp. 313–320, 1984. DOI: 10.1115/1.3239565.

[12] F.K. Moore and E.M. Greitzer, "A Theory of Post-Stall Transients in Axial Compression Systems: Part I — Development of Equations," *ASME Journal of Engineering for Gas Turbines and Power*, vol. 108, no. 1, pp. 68–76, 1986. DOI: 10.1115/1.3239887.

[13] W.G. Joo and T.P. Hynes, "The Simulation of Turbomachinery Blade Rows in Asymmetric Flow Using Actuator Disks," *ASME Journal of Turbomachinery*, vol. 119, no. 4, pp. 723–732, 1997. DOI: 10.1115/1.2841182.

[14] V.H. Garnier et al., "Rotating Waves as a Stall Inception Indication in Axial Compressors," *ASME Journal of Turbomachinery*, vol. 113, no. 2, pp. 290–301, 1991. DOI: 10.1115/1.2929105.

[15] M. Tryfonidis et al., "Pre-Stall Behavior of Several High-Speed Compressors," *ASME Journal of Turbomachinery*, vol. 117, no. 1, pp. 62–80, 1995. DOI: 10.1115/1.2835644.